AEROSPACE REPORT NO.
ATR-2021-02025

Relativistic Proton Spectrometer Detector Calibration

September 27, 2021

M. D. Looper[1], T. P. O'Brien[1], and J. E. Mazur[2]
[1]Space Sciences Department, Space Science Applications Laboratory
[2]Space Science Applications Laboratory, Physical Sciences Laboratories

Prepared for:

JHU/APL
11100 Johns Hopkins Road
Laurel, MD 20723-6099

Contract No. 135557

Authorized by: Engineering and Technology Group

Acknowledgments

The authors acknowledge many useful discussions with members of the Space Science Applications Laboratory and xLAB, as well as members of the Van Allen Probes team.

Abstract

The Relativistic Proton Spectrometer (RPS) was launched in 2012 aboard NASA's Van Allen Probes to measure protons from about 60 MeV to >1 GeV. Especially at the high end of this energy range, where protons typically deposit only a very small fraction of their energy in a spaceflight sensor, making a clean and accurate measurement requires close attention to the calibration of the individual detectors of the sensor. We have used an iterative process to achieve this, performing Geant4 simulations of the sensor to understand its measurements and adjust calibration factors, and in turn using the flight data to improve the simulations. The task was complicated for RPS by its use of a Cherenkov radiator and microchannel plate photomultiplier, whose optical characteristics could not be completely tested and characterized on the ground before flight. This document describes the process by which we determined and improved the calibrations of the individual solid-state detectors and the Cherenkov subsystem of both RPS units, aboard Van Allen Probes A and B. A companion report [4] describes how the multiple detectors' measurements of each recorded particle event are used to identify the species, direction, and energy of the causative particle, and to form energy and angular distributions from the set of protons incident within the sensor's field of view; another companion report [2] discusses the response of RPS to incident electrons.

Contents

Figures

Tables

1. Sensor Configuration and Geant4 Simulations

Two identical Relativistic Proton Spectrometer units, referred to hereinafter as RPS-A and RPS-B, were launched into a near-equatorial geostationary transfer orbit (GTO) aboard the two Van Allen Probes A and B (formerly Radiation Belt Storm Probes). The sensors, their mission, and ground calibrations performed before launch were described by Mazur et al. [3]. The detector complement of each RPS unit comprised a Solid State Detector Assembly (SSDA) with twelve circular silicon detectors and a Cherenkov Radiator Assembly (CRA) with a magnesium fluoride radiator whose light was collected by a microchannel-plate (MCP) photomultiplier "tube" (PMT).

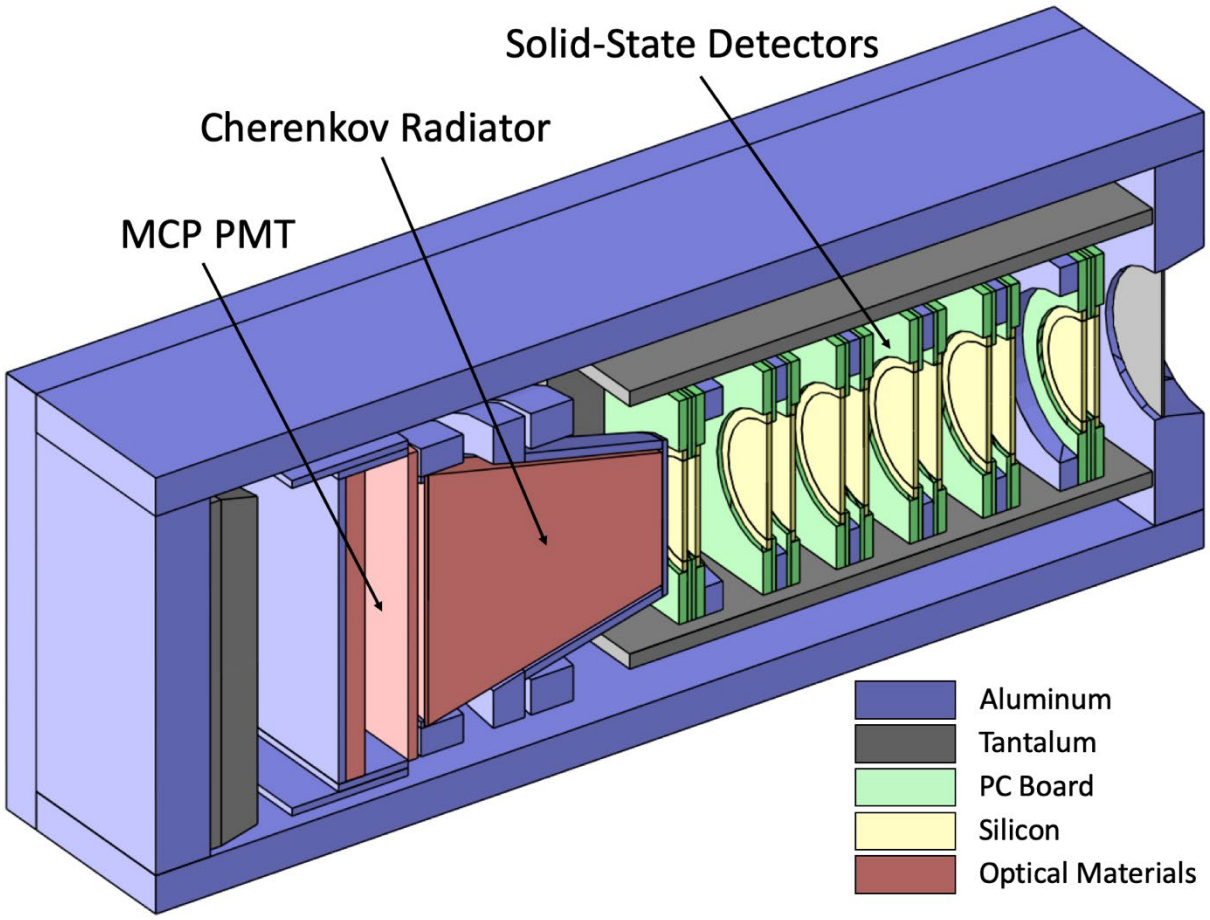

Figure 1. Diagram of RPS active elements and the inert material around them, as simulated with Geant4. Colors identify materials as shown in the legend and discussed in the main text.

Figure 1 is a diagram of the active elements of RPS and of the inert material around them. The instrument was designed to measure protons coming in through the (gray) 20-mil-thick tantalum window at extreme right. The detectors of the SSDA, all of which are 1 mm thick, are lined up behind this window, with particles passing first through two detectors with active areas 20 mm in diameter, A1 and A2. The next eight detectors, numbered D1 through D8 from the one nearest the aperture, have active areas 23 mm in diameter, and the last two are smaller 20-mm detectors again, A3 and A4. Only the eight D detectors were pulse-height analyzed, with their energy deposits being recorded in direct events that were sent to Earth in the telemetry; the A detectors were only used to define an acceptance cone. For an event to be recorded,

the discriminators of a pair of aperture detectors, nominally A1 and A3 (with A2 and A4 as a backup that was never used during the mission), needed to be triggered, along with those of all eight D detectors in between; each detector's discriminator was nominally triggered by 0.2 MeV of energy deposit. The D detectors are larger so that particles traveling in a straight line between the two aperture detectors required by the coincidence conditions would not pass near the outer edges of the active areas of the D detectors, so that the energy deposits therein that were determined by pulse-height analysis would not be underreported due to edge effects.

Behind the SSDA is the magnesium fluoride crystal radiator of the CRA. This was shaped so that the Cherenkov light of relativistic particles coming through the aperture and SSDA would be funneled by total internal reflection to the faceplate of the microchannel plate photomultiplier immediately behind the radiator. The paths of Cherenkov photons generated by relativistic particles going backward through the stack, by contrast, would strike the conical wall of the radiator at angles that would allow many of them to escape and thus not be counted by the PMT. In addition, the small end of the radiator cone was painted black, to further reduce the collection of Cherenkov light from any backward-going particles. The optically active materials in the sensor, comprising the MgF_2 radiator, the fused-quartz faceplate of the PMT, and the microchannel plate behind it, are shown in red. Finally, at the left end of the stack is a tantalum absorber 1 cm thick, to reduce (but, as will be seen below, not eliminate) background from penetrating particles going backward through the stack.

The diagram in Figure 1 was generated by the Geant4 radiation-transport code [1], and represents the geometric model used in our simulations. The tenfold detector coincidence that was required in order for a particle event to be analyzed (elevenfold if the CRA recorded a signal) resulted in response that was very strongly collimated into a double-ended cone defined by the two aperture detectors (A1 and A3), with very little response to particles coming in from the sides. Thus, for the simulations reported herein we did not model the shielding provided by the electronics box around the sensor or by the spacecraft itself, reducing them to an enclosing aluminum box 300 to 450 mils thick to represent the minimum shielding on each side of the detector stack.

As reported by Mazur et al. [3], during the design and ground testing of RPS we performed simulations of its response using Geant4. After launch, once we had measurements of the actual space radiation environment with which to compare those simulations, we found several ways in which we needed to modify the simulations in order to better match the response of the real sensors. These changes, in turn, enabled us to improve our ability to use measured parameters (SSDA energy deposits, CRA Cherenkov light) to reject background events and to determine the original energies of the protons that the instrument was designed to measure. The purpose of this report is to document these changes and to show how they improved our interpretation of the RPS measurements. Mazur et al. [3] presented a table of the physical processes modeled in the simulations, discussing the relevance of each process to the sensors' measurements; Table 1 below is adapted from this, and adds a fourth column to identify the changes that we made to the simulations as documented hereinafter.

Table 1. Physics Processes Included in the Geant4 Simulation of RPS, Describing Modifications Made after Launch. Adapted and Extended from Table 3 of Mazur et al. [3].

Physics process	Relevant to these RPS subsystems	Comments	Changes made to simulation after launch
Electromagnetic energy loss	SSDA (primary measurement); CRA (scintillation); all (transport)	Includes scattering and dE/dx fluctuations for realistic straggling of range and energy deposit	Adjusted SSDA gains to make different detectors' response to the same protons consistent (section 6.1)
Secondary-particle generation	All (transport)	Includes creation of knock-on electrons (delta rays) and bremsstrahlung photons that can carry energy away from detector volumes	None
Nuclear interactions	All (transport)	Based on Geant4 Binary Cascade model	Used average of two smallest SSDA energy deposits to characterize energy deposit, to filter out randomly-occurring large pulse heights that spread out response (section 2.3)
Cherenkov radiation	CRA; MCP faceplate	Photon spectral distributions are shaped by wavelength-dependent refractive index of optical materials	None
Scintillation	CRA	Spectral distribution from Viehmann et al.[6]	Adjusted yield (photons per unit energy deposit) upward from preflight estimate (section 4.2)
Optical photon transport	CRA; MCP faceplate	Includes wavelength-dependent absorption and partial and total internal reflection	Reduced absorption of black paint on small end of CRA radiator to match observed relative suppression of light from backward protons (section 4.1)
Quantum efficiency	MCP photocathode	Wavelength dependence from manufacturer specification	Determined and corrected for variation of overall MCP gain with time and temperature (section 6.2)

For the pre-launch simulations described by Mazur et al. [3] we used version 9.2 of Geant4, with a physics list derived from one of the example user codes provided with the Geant4 package; for the simulations performed after launch and reported herein we used version 10.0 of Geant4, with the QBBC_EMZ reference physics list. In both cases we added optical physics to the list of simulated physical processes in order to model the CRA response. To simulate optical processes like Cherenkov light production, refraction, etc., we needed to define various optical properties like the refractive index as a function of photon wavelength for transparent materials; the selected values of such properties, and where we obtained them, are detailed in the Appendix. This enabled Geant4 to simulate the production in these materials of optical photons (which it treats as a separate kind of particle from ionizing radiation in the form of X-ray and gamma-ray photons, whose transport Geant4 simulates with a completely different

set of physical models) by Cherenkov light and scintillation and also their attenuation due to imperfect transparency, and the refraction or reflection of optical photons at boundaries between these materials and the surrounding vacuum. (The MCP itself is made of a proprietary glass formula, but since we did not take account of any photons that reached it, we just used quartz to approximate the tiny amount of inert shielding that it added behind the detector stack.)

The response of fully-depleted solid-state detectors is straightforward to simulate: one simply sums up the energy deposited by particles as they traverse or stop in the active volume of the detector. Recent versions of Geant4 can be set up to do this with just a few lines of user code, by means of software-defined "primitive scorers." In addition, Aerospace has flown silicon solid-state detectors since very early in the Space Age, and we have a long understanding of how to bias them, how to calibrate them, how to read them out, etc. By contrast, we were not equipped to test in a lab such parameters of the CRA optical system as spatial uniformity of response and quantum efficiency vs. wavelength of the PMT, and in any case it is not obvious how to model the response of a PMT using physical processes available in Geant4. This meant that we had to make what we thought were reasonable assumptions to build our model; comparison reported hereinafter of the simulation results with flight data showed that the basic assumptions were reasonable, but also showed us where we needed to make adjustments to the details, as described in sections 4 and 5.

To represent the detection of photons by the PMT in the simulations, we used a different kind of Geant4 primitive scorer to count simulated optical photons entering a thin box representing the photocathode on the back of the faceplate. Before counting a photon that reached the photocathode, however, we represented the nonuniformity of response across the faceplate by applying a random particle deletion with a probability defined by the position of the photon, and we represented the quantum efficiency by applying another random deletion with a probability defined by the wavelength of the photon. Our assumptions about nonuniformity and quantum efficiency are also discussed in the Appendix. In the output of the simulations, then, each particle event that satisfied the coincidence conditions (at least 0.2 MeV of energy deposit in A1, A3, and D1 through D8) was recorded in the output file with twelve solid-state detector energy deposits and one number of photons counted by the PMT.

2. Simulated Detector Response

2.1 Solid-State Detectors

A typical solid-state-detector range/energy-deposit telescope will determine the species and energy of particles entering its aperture by analyzing the energy deposits in all detectors that each particle reaches, as well as the maximum depth (number of detectors) reached by the particle before it comes to a stop. Since RPS was intended to measure protons up to very high energies, which can penetrate meters of aluminum (or silicon), we made no provision for the analysis of stopping particles, but instead set its coincidence conditions so that we only receive data for events passing through the entire pulse-height-analyzed stack of SSDA (D1 to D8). We thus give up the measurement of particle range and have only the energy deposits in the eight detectors (plus possibly a photon count from CRA, discussed below).

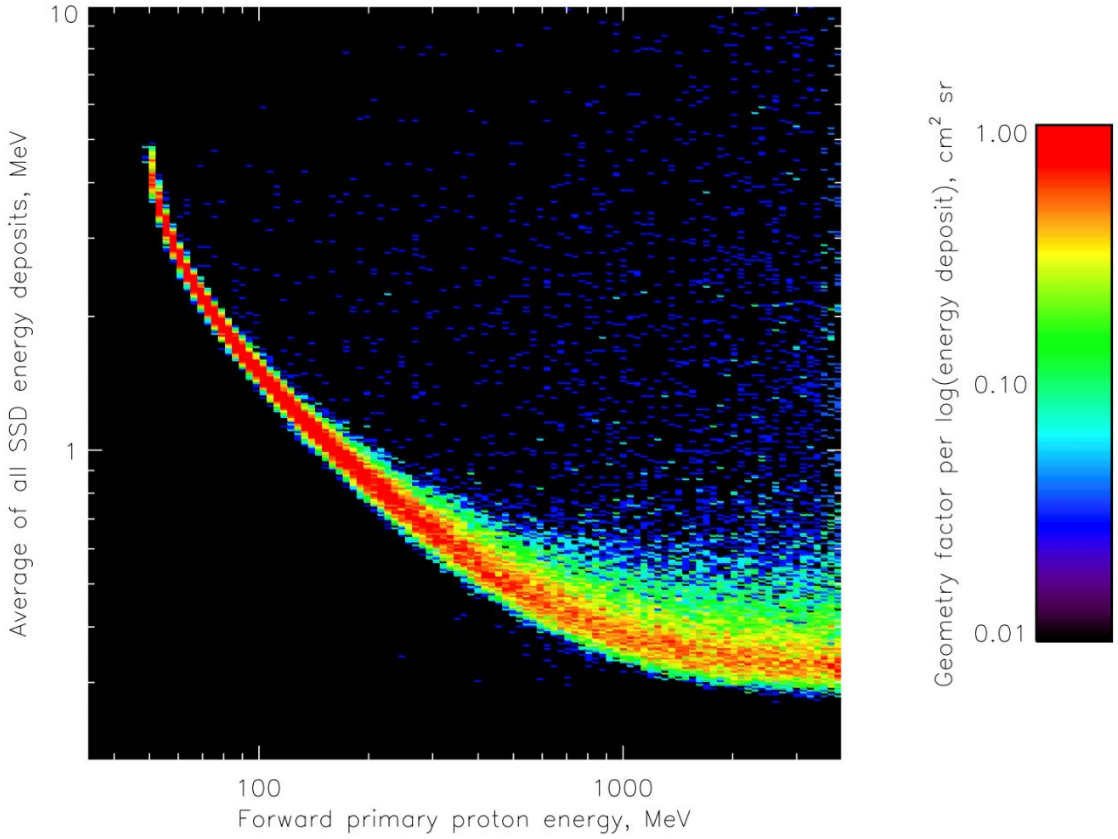

Figure 2. Distribution of the average of all simulated energy deposits in D1 through D8 as a function of the incident proton energy, for protons reaching the sensor from the hemisphere centered on the direction of a particle entering the aperture parallel to the axis of the detector stack. Colorscale is effective geometry factor for events falling in each energy-deposit bin, normalized to the logarithmic width of the bin.

The simplest way to use data from the SSDA is just to look at the average energy deposit in the eight detectors. Figure 2 shows the probability distribution of this average energy deposit as a function of the energy of simulated protons illuminating the sensor geometry in Figure 1. This plot only considers "forward" protons, i.e., those from the half of the 4π sr sphere of incidence directions that have a positive velocity component in the direction of particles entering the aperture. As noted above, this response is strongly collimated about the axis of the detector stack within the A1/A3 acceptance cone, but the whole

hemisphere of incidence directions and the whole surface of the geometry in Figure 1 are illuminated for completeness. The quantity represented by the colorscale in Figure 2 is the effective geometry factor, differential in the logarithm of the energy deposit; an integral of the values along each vertical cut through the plot would add up to a sum close to the nominal straight-lines geometric factor of the acceptance cone, 0.136 cm^2 sr. The quantity measured by the real sensor was the solid-state detector energy deposits; to use this observable to determine the energy of the causative primary proton, we would draw a horizontal line on this plot to see what proton energies might produce a given event's observed energy deposit. This works well up to a couple of hundred MeV, but as the curve bends toward the horizontal and widens in the vertical direction due to the generation of numerous secondary particles by electromagnetic or nuclear interactions of the proton with the sensor's materials, we see that a wide range of primary proton energies can cause events with energy deposits of around 0.3 to 0.5 MeV, so that the energy resolution of a spectrometer analyzed in this way would become very poor at these higher energies.

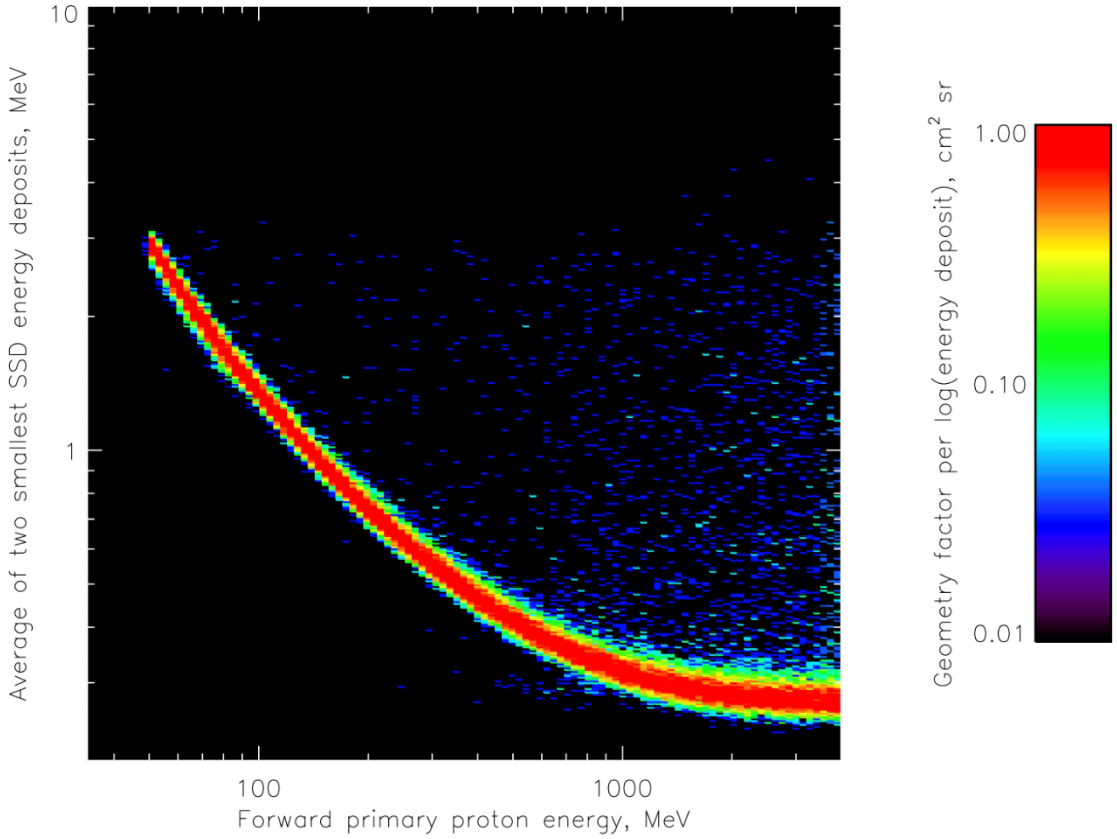

Figure 3. Distribution of the average of the two smallest energy deposits among the eight detectors D1 through D8, as a function of the energy of simulated protons incident over the forward hemisphere as in Figure 2.

Following a suggestion from the late Norm Katz, Figure 3 shows the average only of the two detectors among D1 through D8 with the lowest energy deposits in a given event, instead of the average among all eight detectors ("minimum-two"). This makes little difference at lower primary proton energies, but by discarding the contributions of detectors with additional energy deposits due to secondary particles, it considerably tightens up the area that displays substantial response toward the right end of the curve. In turn, this means that a narrower range of primary proton energies are likely to have caused an event with a given minimum-two energy deposit, improving the accuracy of the primary proton energy estimated from

this observable. As detailed by O'Brien et al. [4], this was the method that we used to extract primary proton energies from the observations in flight.

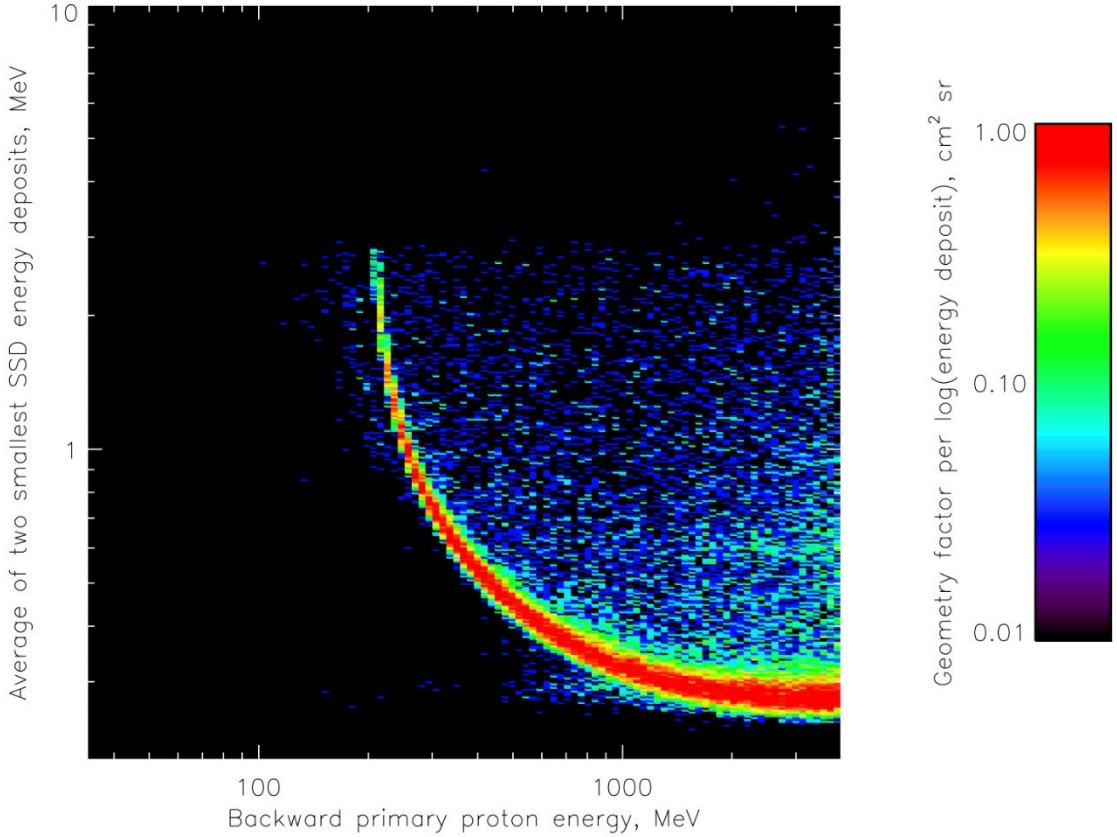

Figure 4. Distribution of the average of the two smallest energy deposits among the eight detectors D1 through D8, as a function of the energy of simulated protons incident over the backward hemisphere opposite that in Figures 2 and 3.

One limitation of a space radiation sensor consisting of a solid-state detector telescope is that, for high enough energies, it is difficult to distinguish which way a penetrating particle is going through the telescope. If the energy lost in passing through the telescope is small compared to the particle energy, then all detectors of the telescope will measure essentially the same pattern of energy loss (same mean, same fluctuations) for such particles going through the stack in either direction. Figure 4 shows the distribution of minimum-two energy deposit as a function of primary proton energy, for arrival directions over the backward-going hemisphere of directions omitted from Figures 2 and 3. Even though a proton coming into the backward acceptance cone defined by D1 and D3 must pass through the back of the electronics box, 1 cm of tantalum, and the entire CRA in order to reach the stack, we see response starting around 200 MeV, and there are many such protons in the inner zone to add background to the forward measurements. As noted, at the highest energies the pattern of energy deposits in the solid-state detectors from backward protons becomes indistinguishable from that of forward protons; rejecting backward-going protons is the main obstacle to making accurate measurements of the highest-energy geomagnetically trapped protons, beyond several hundred MeV in energy, and was the reason for inclusion of the Cherenkov radiator assembly in RPS.

2.2 Cherenkov Subsystem

Unlike most solid-state detector telescopes flown in space, RPS has a Cherenkov radiator to extend energy resolution and directional discrimination to higher energies than are possible with a detector stack like SSDA alone. A proton of a given energy will produce the same amount of Cherenkov light regardless of which direction it goes through the radiator crystal; however, as discussed in section 1, the CRA was designed to enhance collection of light from forward-going protons and to suppress collection of light from those traveling backwards through the radiator and the SSDA stack.

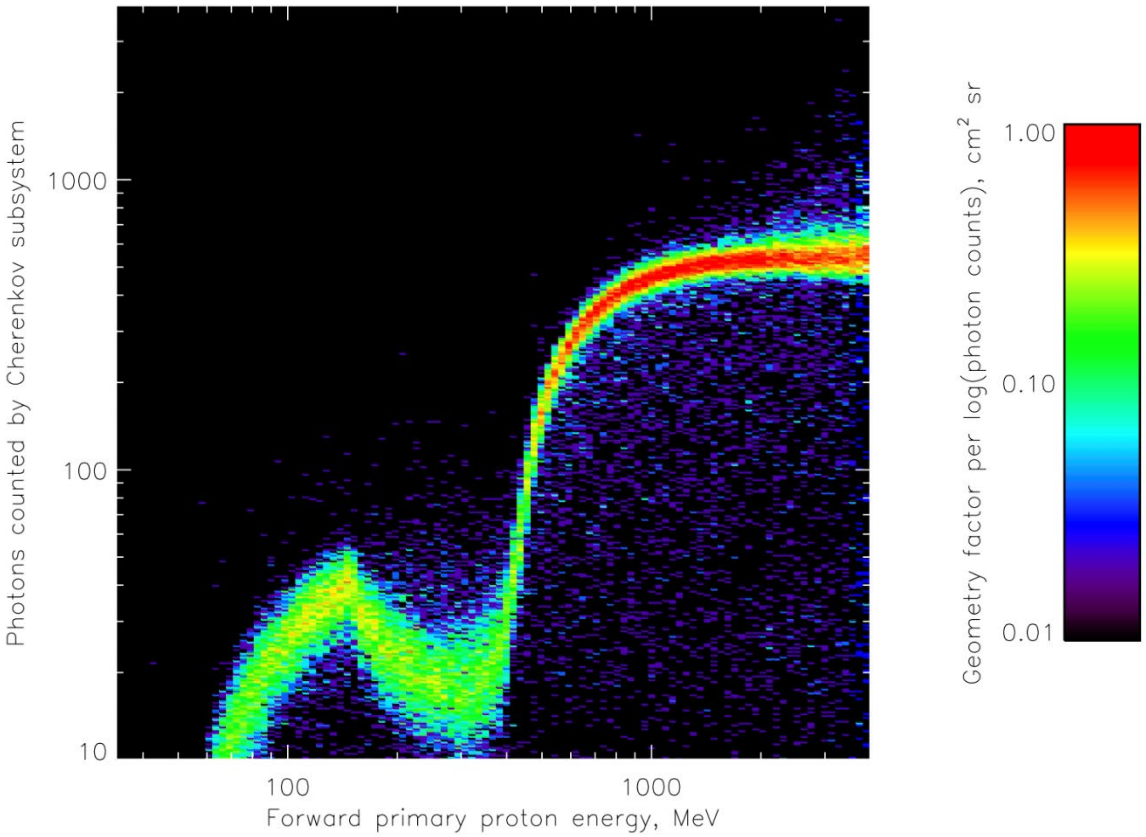

Figure 5. Distribution of number of photons counted by CRA, as a function of the energy of simulated protons incident over the forward hemisphere as in Figures 2 and 3.

Figure 5 shows the response of the simulated CRA, with the assumptions about optical parameters as detailed in the Appendix, for protons arriving over the forward hemisphere as in Figures 2 and 3. Again, the colorscale is the geometric factor for events with a given primary proton energy that fall in each photon-count bin, differential in the logarithm of the number of counts. Cherenkov light is produced by relativistic particles when their speed is faster than the speed of light in a transparent medium; this accounts for the sharp rise with proton energy in the number of photons counted starting at about 400 MeV. Below this threshold energy, as discussed by Mazur et al. [3], we saw evidence of Cherenkov light being produced by energetic secondary electrons (delta rays), and also by scintillation produced by ionization energy deposited in the crystal. The contribution of delta-ray Cherenkov light relative to such light from primary protons is fixed by the optical and other properties of the material, but the intensity of scintillation is a free parameter; in preflight measurements we estimated that 5 scintillation photons would be produced per MeV of energy deposit, but the simulation shown in Figure 5 has 16 photons per MeV in

order to make its effect more readily visible (and, as discussed in section 4 below, examination of the flight data led us to conclude that the actual value was even higher).

As proton energy goes up, the amount of ionization energy deposit rises up to a point, as the proton comes to a stop in the crystal with more and more energy left to deposit after passing through the SSDA. Around a primary proton energy of 150 MeV, the proton is energetic enough to pass all the way through the crystal, and so its energy deposit falls since dE/dx falls with increasing proton energy and pathlength is maximized at the length of the crystal. Going higher in primary-proton energy, we see a fuzzy transition due to Cherenkov light from delta rays, and then the sharp rise in light output where the proton itself starts to emit Cherenkov light. Finally, at the highest energies where the proton speed approaches that of light (in vacuum), the Cherenkov light signal saturates as the maximum yield per unit pathlength is produced along the maximum pathlength through the entire crystal.

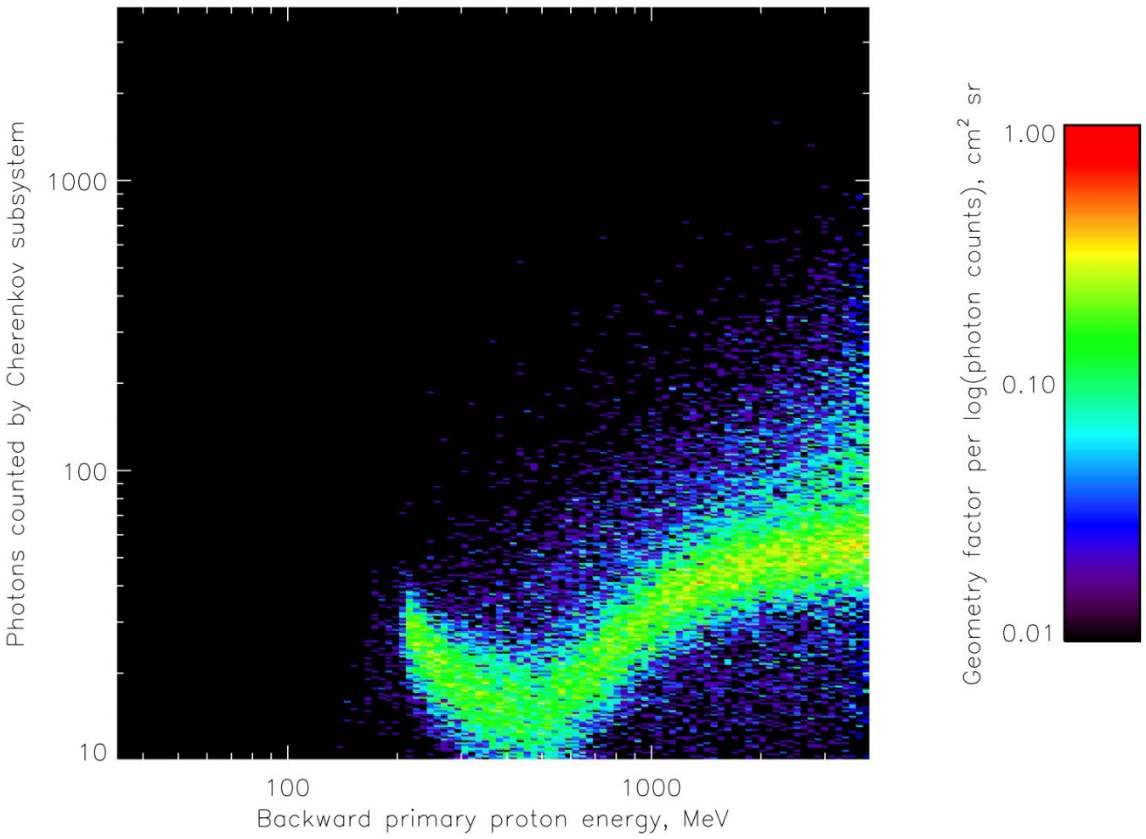

Figure 6. Distribution of number of photons counted by CRA, as a function of the energy of simulated protons incident over the backward hemisphere as in Figure 4.

Figure 6 shows the distribution of simulated CRA photon counts as a function of the energy of backward-going protons. As in Figure 4, there is a threshold at about 200 MeV primary proton energy, which is the minimum to get through the electronics box, tantalum absorber, CRA, and the entire SSDA stack to trigger detector A1. This is of course well above the energy needed to penetrate the radiator crystal, so the scintillation response falls as proton energy increases from there, and when the Cherenkov light begins to rise we see that, as designed, the light collected by the PMT is much lower than for forward-going protons in Figure 5. This will enable us to separate and reject energetic backward-going protons whose SSDA

signature is indistinguishable from that of the energetic forward-going protons that RPS was flown to measure.

2.3 Combined Response

Of course, in the flight data we cannot directly sort out observable properties of measured particle events by the energy of the protons causing them, as in Figures 2 through 6; rather, we see the aggregate of the observables for each event and try to deduce from them the properties of the causative particles. To simulate the observations, we need to assume a set of properties for those particles and then fold them through calculations like those above. For the simulation figures below, we modeled an environment consisting of isotropic protons, and we assumed an energy spectrum based on an estimate of the daily average that was made early in the mission. That estimate relied on early versions of the calculations herein, of course, and so we could iterate with later-modified simulations to improve it. However, for purposes of this section, we just want to get the balance of different parts of the response (high-energy backward protons, low-energy forward protons, …) approximately right so that the overall pattern is recognizable when we compare it with observations, and so we did not iterate to re-create these plots with a better estimate of the spectrum.

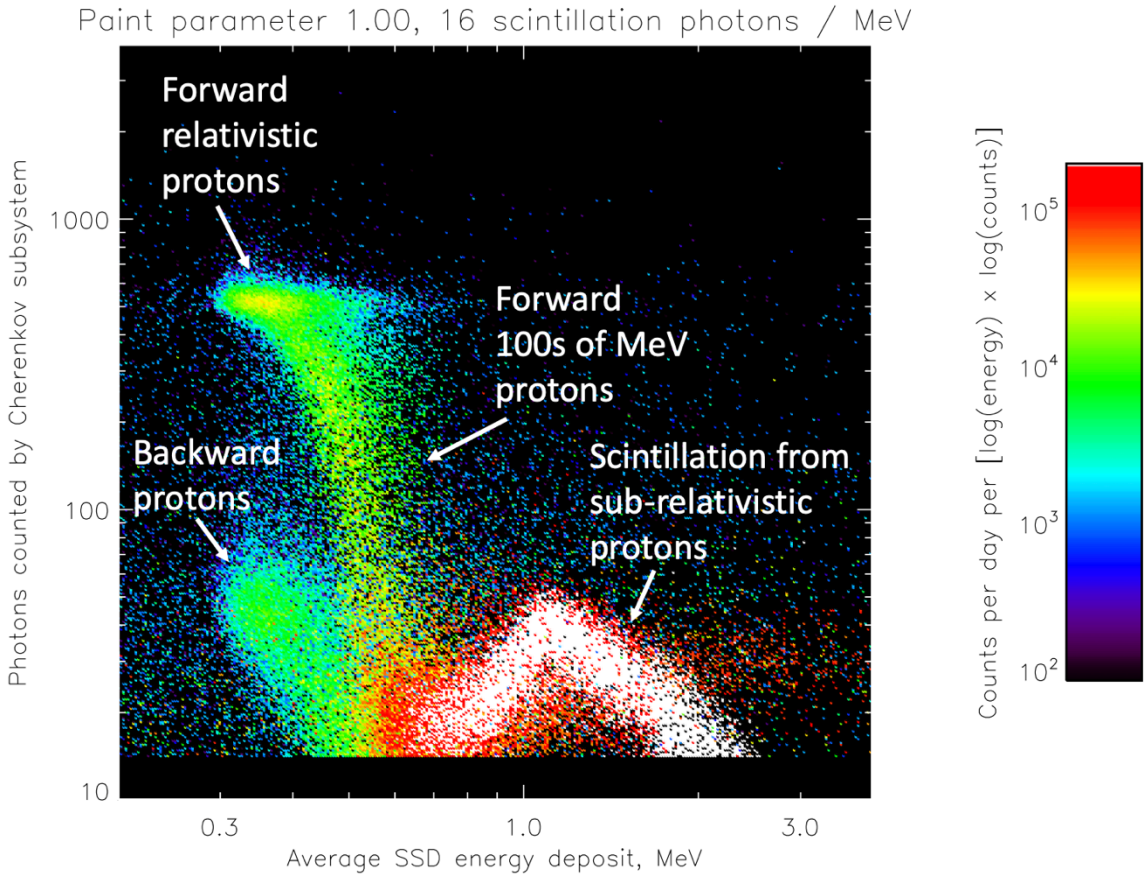

Figure 7. Distribution of Cherenkov counts vs. average energy deposit in all eight SSDs, for simulated events due to isotropic protons with a spectrum approximating the daily average early in the mission. Colorscale displays rate per bin, differential in the logarithm of energy deposit and the logarithm of photon counts.

Figure 7 shows the result of such a convolution, plotting the expected distribution of photon counts vs. the average of energy deposits in all eight pulse-height-analyzed detectors D1 through D8. The energy deposit due to protons declines with higher primary proton energy, so the contributions due to forward and backward protons resemble the distributions in Figures 5 and 6 flipped about a vertical axis. In particular, the red/white chevron due to scintillation is visible around 1 MeV energy deposit, and the sharp increase with proton energy of forward Cherenkov output forms a band rising toward the upper left. Since Cherenkov light saturates at a high level and SSD energy deposit at a low level as proton energy rises, the highest-energy protons' events are concentrated in two blobs around an energy deposit of 0.35 MeV, a higher one for forward protons and a lower one for backward protons. The title at the top of the plot is included for later reference; the number of scintillation photons per MeV of energy deposit in the Cherenkov radiator and a scaling factor associated with the black paint on the tip of the radiator are both parameters that we will adjust in section 4 so that the simulation results better match the flight data.

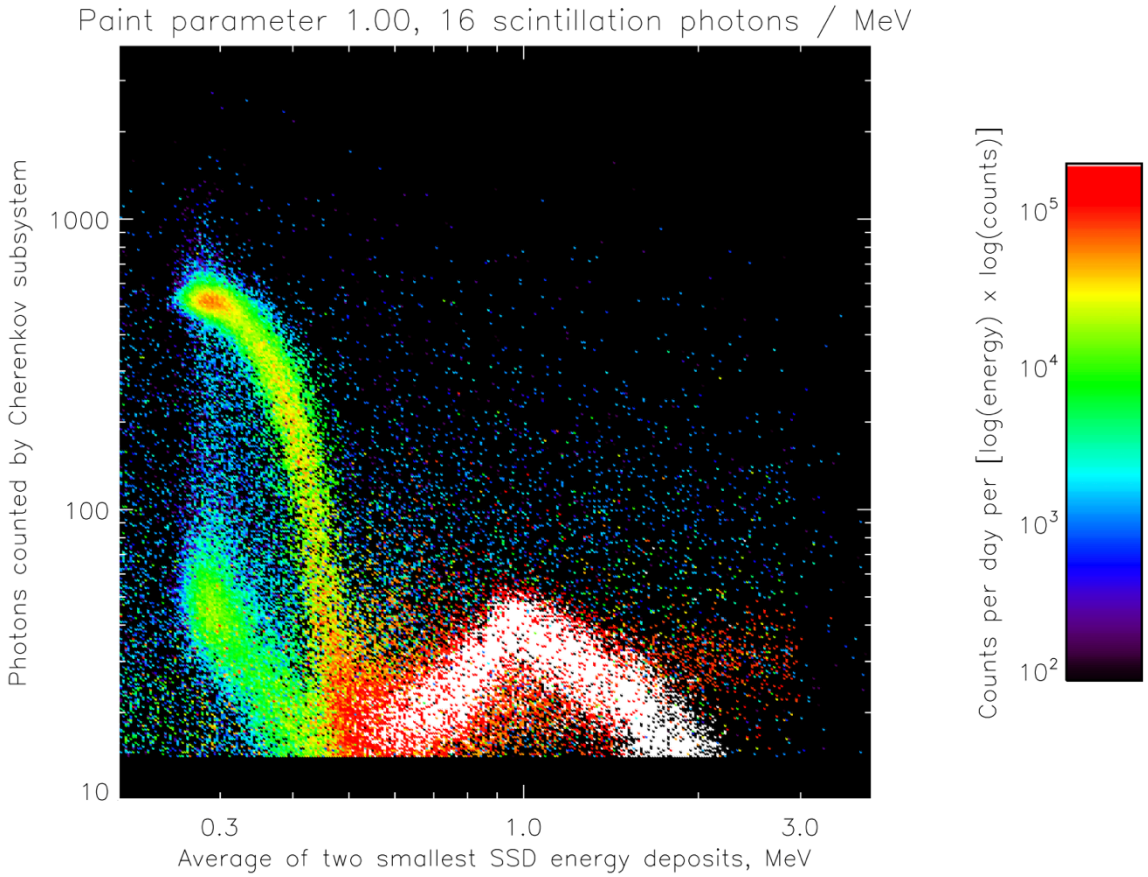

Figure 8. Distribution of Cherenkov counts vs. average of two smallest energy deposits per event in D1 through D8, for simulated events due to isotropic protons with a spectrum approximating the daily average early in the mission.

If we represent the SSDA output not by the average of all eight detectors' energy deposits as in Figure 2 but by the minimum-two value as in Figure 3, the distribution of points tightens up considerably as shown in Figure 8. In particular, the forward and backward bands of points with low but nonzero Cherenkov light, which meet around a minimum-two energy deposit of 0.45 MeV, are better separated here than in Figure 7. This will improve our ability to distinguish between forward and backward protons where it is hardest to do so and thus to minimize background in the measurement of forward protons.

3. Initial Conversion of Detector Telemetry Values to Physical Units

3.1 Solid-State Detectors

As noted above, Aerospace has long experience with building and flying silicon solid-state detectors, so their calibration is generally well understood. In the case of RPS, we mounted a small alpha-particle source above a small extension of each detector D1 through D8 outside their main circular active areas [3], so that we could track any changes in the detectors' gains that occurred over the mission. The eight SSD pulse heights in a particle event reported in the telemetry will be integers, analog-to-digital converter (ADC) channels from on-board digitization of the current pulse due to ionization energy deposited in the detector. Based on the two distinct energies of the alpha particles emitted by the onboard sources and the ADC channels in which they were counted, we derived the following formula that scales the ADC pulse heights H_i for detector i linearly to report a set of energy deposits D_i in MeV, with a further adjustment that is linear in daily-averaged temperature $\bar{T}(t)$, and with gains and offsets g_i and c_i as given for the detectors of each RPS unit in Table 1:

$$D_i = \frac{c_i + H_i g_i}{T_0 + T_1 \bar{T}(t)}$$

$$D_i = \text{Deposit in } i^{\text{th}} \text{ SSD, MeV}$$
$$c_i = \text{Offset for } i^{\text{th}} \text{ SSD, MeV}$$
$$g_i = \text{Gain for } i^{\text{th}} \text{ SSD, MeV/channel}$$
$$H_i = \text{Pulse height for } i^{\text{th}} \text{ SSD, channel}$$
$$T_0 = 1.02 = \text{Temperature correction offset}$$
$$T_1 = -6.22 \times 10^{-4} = \text{Temperature correction slope, } 1/℃$$
$$\bar{T}(t) = \text{Daily-averaged temperature, } ℃$$

Table 2. SSDA Gains and Offsets Determined from Alpha Source Measurements, in Units of MeV/Channel and MeV Respectively

Detector	RPS-A gain	RPS-A offset	RPS-B gain	RPS-B offset
D1	0.006463	0.04268	0.006482	0.04911
D2	0.006479	0.04484	0.006482	0.05277
D3	0.006464	0.04417	0.006523	0.01424
D4	0.006477	0.04356	0.006479	0.05312
D5	0.006450	0.04407	0.006496	0.04865
D6	0.006463	0.04642	0.006483	0.05197
D7	0.006470	0.04047	0.006482	0.04964
D8	0.006460	0.04459	0.006482	0.04720

3.2 Cherenkov Subsystem

The output of the Cherenkov subsystem was reported for each event returned in the telemetry as an ADC channel from onboard digitization of the charge liberated by photons from the photocathode and amplified by the microchannel plate. The current pulse produced in a solid-state detector can be related in a fairly straightforward way to the energy deposit, based on electronic parameters such as the capacitance of the detector, the ionization potential of silicon, etc.; the amplitude of the charge pulse at the output of the CRA photomultiplier, on the other hand, is related to the properties of the particle traversing the

radiator crystal by numerous details of the optical processes and of the MCP behavior for which we only have estimates, and moreover a comparison of preflight ground data with in-flight measurements from early in the mission showed that the gains had shifted during launch. Fortunately, nature provided us with two points that we could use, with some assumptions, to determine a linear scaling from the ADC channel to the number of photons counted for each RPS unit; initially, we did not determine a temperature correction for the CRA, though this was later done as described in section 6.2.

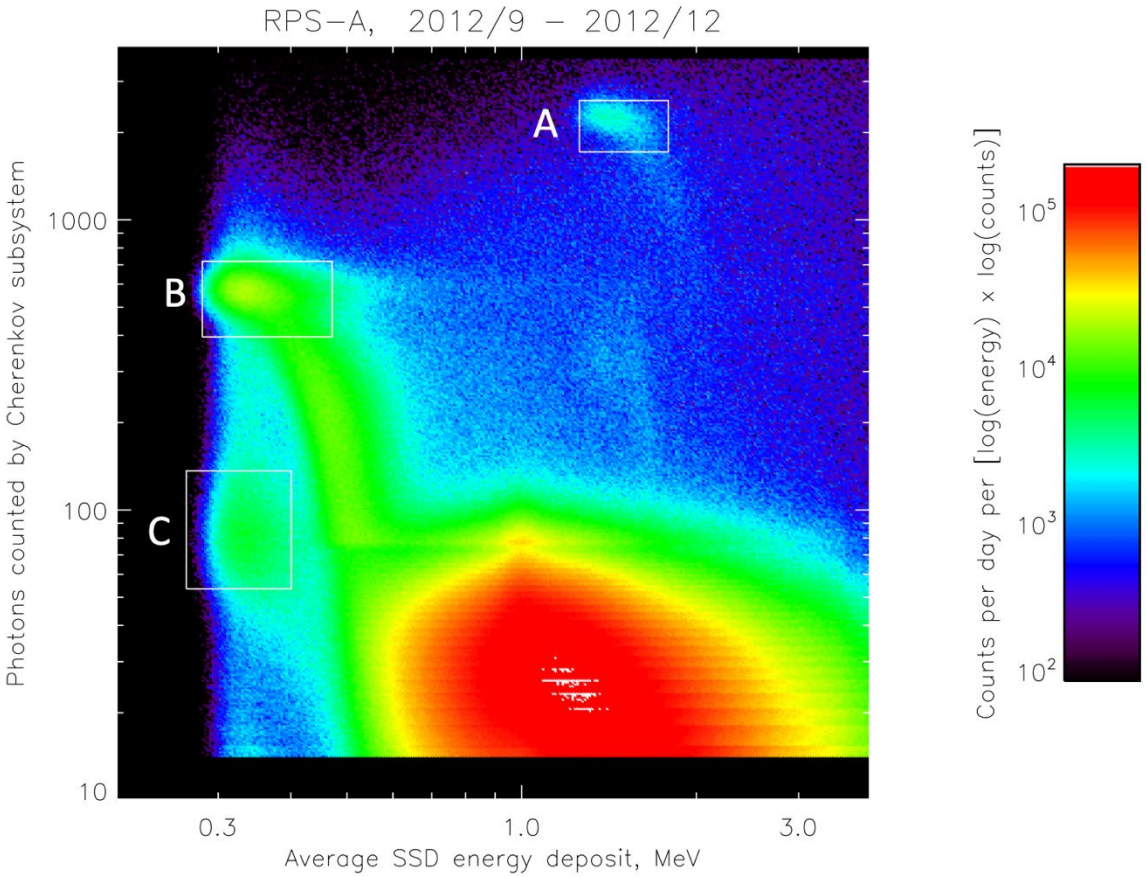

Figure 9. Distribution of Cherenkov counts vs. average energy deposit in all eight SSDs, from RPS-A observations during the first four months of the Van Allen Probes mission. Labeled boxes show regions in which distributions of CRA PHA values were analyzed to determine the conversion from PHA values to photons counted, as described in the text.

Figure 9 is a plot like Figure 7, showing the distribution of events in Cherenkov photons counted vs. average energy deposit in D1 through D8, but for RPS-A data at the start of the mission. The forward and backward mid- and high-energy proton portions look fairly similar to the simulated ones in Figure 7, but it is clear that the distribution of scintillation light is much broader in the real instrument than in the simulation. (The horizontal striping is due to "beating" between the finite-width CRA PHA channels and the logarithmic bins into which events were sorted to make the plot; the slight discontinuity at about 80 photon counts is due to a transition between differently-weighted telemetry buffers that sort events with larger and smaller CRA pulse heights, as discussed by O'Brien et al. [4].) Early on we started calling such diagrams "Nessie plots," after the Loch Ness monster, with the scintillation region forming the body,

forward intermediate energies with some Cherenkov light forming the neck, and the forward saturated spot forming the head.

The labeled boxes in Figure 9 show the exact regions that we used to determine the scaling between PHA values and photon counts. Fortunately, the gain of the MCP in RPS-A was low enough that the full-scale range encompassed not only the full dynamic range of light caused by protons, but also that caused by energetic ^{4}He ions. The protons making up this plot encompass the inner-zone population, which has a spectrum that falls with increasing energy, and the galactic cosmic rays (GCRs), whose spectrum peaks at hundreds of MeV per nucleon; thus both the scintillation-dominated part of the plot and the relativistic "neck" and "head" are populated. The helium population of the inner zone, on the other hand, is mostly below the energy range measured by RPS, and so what we see in this plot is the contribution of relativistic and near-relativistic GCR helium. Both Cherenkov light and SSD energy deposit are four times larger for ^{4}He than for ^{1}H at a given energy per nucleon, so we see the forward helium head in the box labeled "A" in Figure 9, which we can take to have four times the Cherenkov light of the forward proton head at "B". (A backward helium head, corresponding to the backward proton head at "C", is faintly visible below "A" as well.). Equating the mean PHA channel of events in box "B" with the mean photon count in the corresponding part of the simulation in Figure 7, and equating the mean PHA channel of events in box "A" with four times this value, gives us a linear relation between PHA channel and photons counted for the CRA of RPS-A (which has then been applied to the PHA channels in creating Figure 9 so that the vertical scale is the same as in the simulations). The gain and offset, analogous to those for SSDA in Table 1 above, are given in Table 2.

$$D_9 = c_9 + H_9 g_9$$
$$D_9 = \text{CRA photon count}$$
$$c_9 = \text{Offset, photons}$$
$$g_9 = \text{Gain, photons/channel}$$
$$H_9 = \text{Pulse height for CRA, channel}$$

Table 3. CRA Gains and Offsets, in Units of Photons/Channel and Photons Respectively

Parameter	RPS-A	RPS-B
c_9	7.42765	8.705149
g_9	2.649163	0.7694737

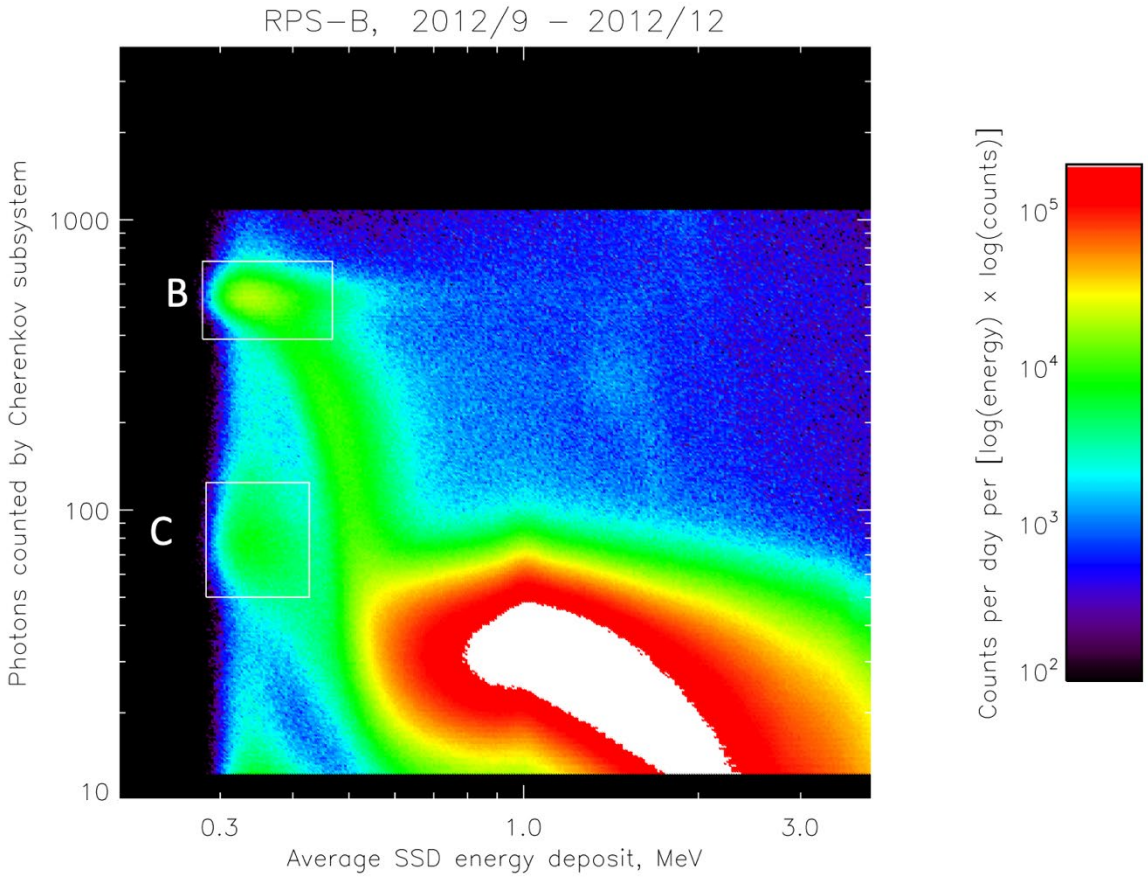

Figure 10. Distribution of Cherenkov counts vs. average energy deposit in all eight SSDs, from RPS-B observations during the first four months of the Van Allen Probes mission.

Figure 10 shows the same distribution as in Figure 9 of particle events from RPS-B. The distribution of scintillation light is noticeably tighter in the vertical direction than for RPS-A, and the gain is substantially higher so that the forward helium head is off-scale. To determine the coefficients in Table 2 for RPS-B, we had to make the assumption that the collection of forward and backward Cherenkov light was similar to that in RPS-A, and therefore that the mean number of photon counts in the backward proton head "C" in relation to that of the forward head "B" would be the same for both RPS units. This should be independent of any differences in scintillation between the two units' radiators, because the lower energy deposit in the radiator as well as in the SSDs means that Cherenkov light will be the dominant contribution in both forward and backward heads. Equating the mean PHA value in box "B" with the mean number of counts in the corresponding part of the simulated event distribution in Figure 7, and assuming that the ratio between the mean values in boxes "B" and "C" is the same as in Figure 9, we derive the linear coefficients for RPS-B shown in Table 2.

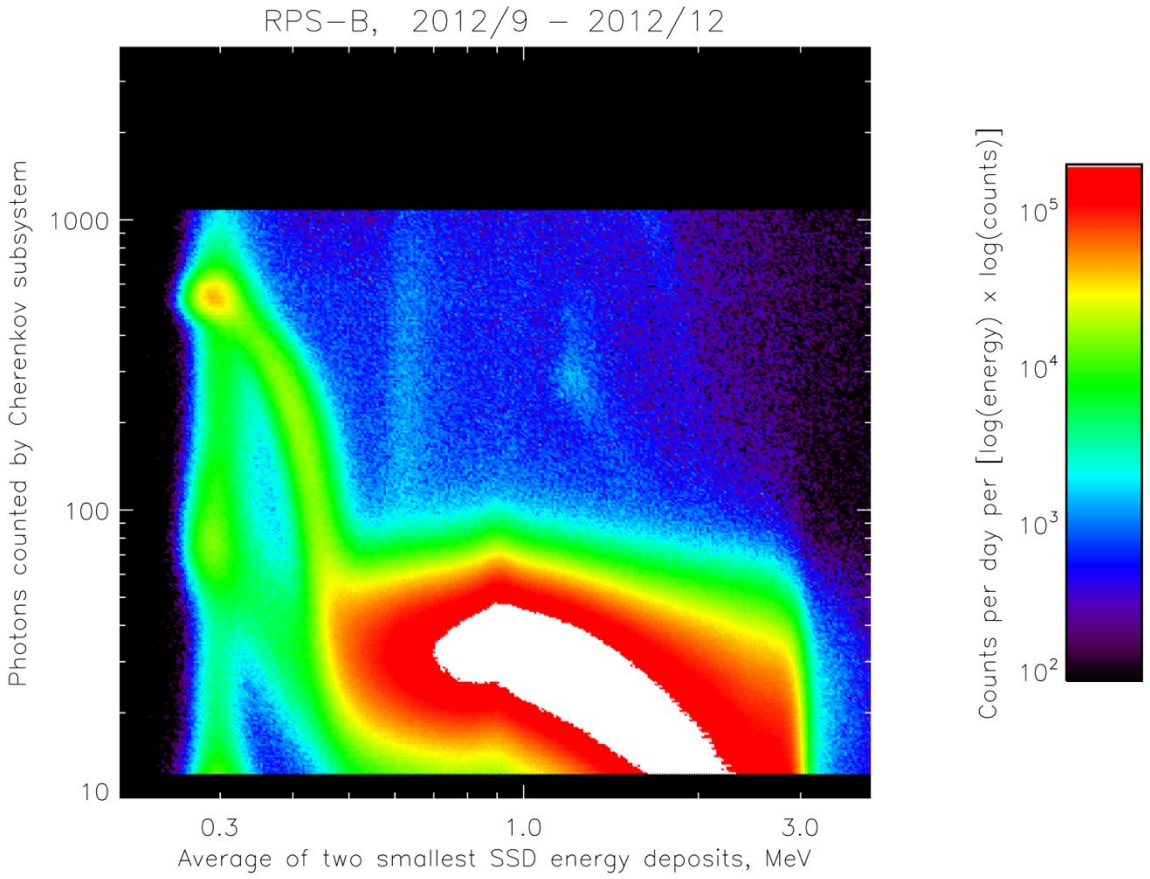

Figure 11. Distribution of Cherenkov counts vs. average of the two smallest energy deposits in D1 through D8, from RPS-B observations during the first four months of the Van Allen Probes mission.

As noted in the discussion of Figure 8 above, using the average of the two smallest energy deposits in D1 through D8 for a given event, instead of the average energy deposit in all detectors, tightens up the distribution of events considerably. Figure 11 shows a "Nessie plot" of the same data as in Figure 10, but with the SSD signals mapped to the minimum-two value for each event rather than the average. As between Figures 7 and 8, this improves separation between forward and backward protons where their distributions come together at the base of the "necks"; it also improves definition of other background populations, like geomagnetically trapped multi-MeV electrons (see [2] for further discussion) that form a vertical band through the two proton heads, or the backward head and forward neck for GCR helium, or the vertical band at about 0.6 MeV that is due to two delta rays traversing the detector stack after a causative primary proton has generated them in the inert material in front or in back of it (this attribution was determined by examining what primary and/or secondary particles crossed each detector in the simulations). The improved visibility of these background populations when sorted by minimum-two SSD energy makes it easier to reject them from our analysis of the forward protons, and as noted above we have used this for all analyses since fairly early in the mission; Figures 9 and 10 show the average of all eight SSDs only because that is what we used to determine the calibration in Table 2 at the start of the mission.

4. Adjustment of Optical Parameters of Simulated CRA

4.1 Absorption of Paint on Tip of Radiator

A comparison of the flight data in Figures 9 to 11 with the simulation results in Figures 7 and 8 will show that the backward proton head is noticeably higher in the real data than in the simulations; that is, the real CRA is not quite as effective at suppressing the collection of Cherenkov photons from backward-going protons as the simulations had assumed. (This is why we used the ratio between observed counts in the forward and backward heads to determine the calibration of the CRA in RPS-B, rather than equating the value in the backward head with that in the simulation.) It is not obvious what the simulation is getting wrong; however, since we are interested in the backward-going light only for purposes of identifying and eliminating backward-going events, not for purposes of quantifying them, we decided to adjust the effectiveness of the absorption of the black paint on the small end of the radiator in the simulations to see if we could get a better match. This would have little effect on the light from forward protons, which would mostly go directly to the PMT.

The "paint parameter" mentioned in the title of the plots in Figures 7 and 8 is the ad hoc variable that we used to tune the backward light collection. More recent versions of Geant4 have the option to assign optical parameters (diffuse reflection, specular reflection, transmission) to simulated surfaces that are tabulated from measurements of real sample materials; however, this was not available early in the Van Allen Probes mission when we were running these simulations, and so we represented the black paint on the small end of the radiator by a thin disk of "black MgF_2." This was an artificially-defined material with the same profile of refractive index vs. wavelength as that of real MgF_2 (see Appendix), but with a very short absorption length. The equality of refractive indices meant that a photon heading across the small end of the radiator crystal would pass directly into the "paint," with no internal reflection, and it would then be quickly absorbed. The "paint parameter" was a multiplicative scaling factor applied to the refractive index in the "black MgF_2" such that 1.00 gave a refractive index profile vs. wavelength that was the same as real MgF_2 and 0.00 was unity at all wavelengths, like vacuum. Thus a parameter of 1.00 meant that photons going through the small end of the radiator would enter the "black MgF_2" and disappear due to the short absorption length, while a parameter of 0.00 meant that the same fraction would be internally reflected as if there were vacuum on the other side (and the rest would disappear).

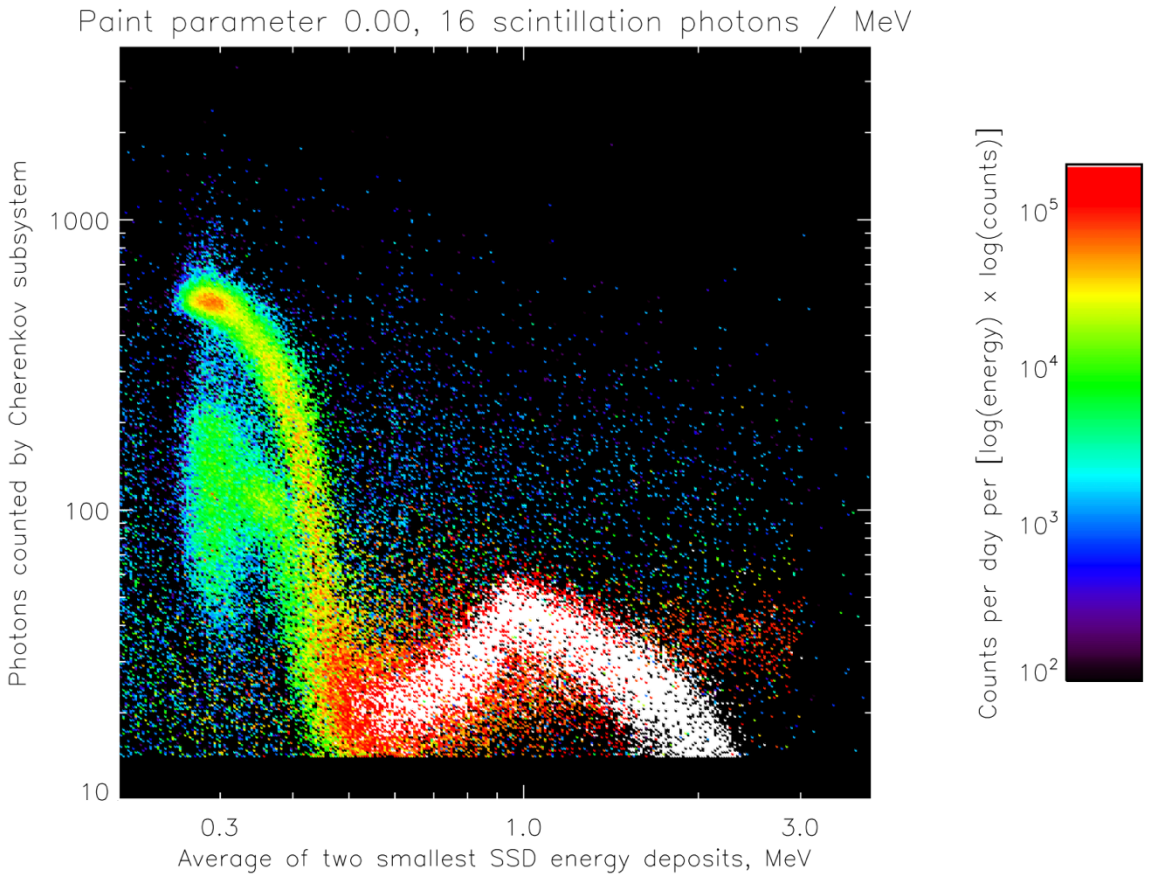

Figure 12. Distribution of Cherenkov counts vs. average of two smallest energy deposits per event in D1 through D8, for simulated events due to isotropic protons with a spectrum approximating the daily average early in the mission. This is the same plot as in Figure 8, but with a paint parameter of 0.00 rather than 1.00.

Figure 12 shows the result of changing the paint parameter to 0.00 from 1.00 as in Figure 8, and as our first simulations without an adjustable parameter implicitly assumed. As expected, the forward head and neck and the scintillation-dominated region are little changed, but the backward head and neck have much more light recorded by the PMT. Comparing with observations as in Figure 11, we see that there is now too much backward light in the simulation, and that the backward head is also much broader vertically than in the flight data. Running simulations with different values and comparing with the data, we finally arrived at a value of 0.45 as the best match. This is a completely ad hoc adjustment rather than a physically derived parameter like those in the Appendix, but it does represent a physically reasonable process, namely imperfect absorption of incident light by the black paint. Since, again, the goal is not to quantify the response of RPS to backward-going events but only to identify that response so we can reject such events, we judged that it was sufficient for the purpose.

4.2 Scintillation Yield in Radiator

As discussed Mazur et al. [3], based on comparisons of simulations with pre-flight ground testing data, we estimated that 5 scintillation photons were produced per MeV of energy deposit in the MgF_2 radiator. As detailed in the Appendix, we adopted a spectral distribution for the simulated scintillation photons from Viehmann et al. [6], who estimated a yield of 20 photons per MeV for UV-grade MgF_2. The events

in the flight data shown in Figure 11 that display the effects of scintillation most strongly are concentrated in the white "wing" (transforming Nessie into a swan, perhaps) that mirrors the white chevron peaked around 1 MeV minimum-two energy deposit in Figure 12. The vertical position of this region in the flight data is similar to its position in Figure 12, with over three times as much scintillation yield as we had estimated before flight, indicating that the real value is more in line with that of Viehmann et al. [6] than with our original estimate.

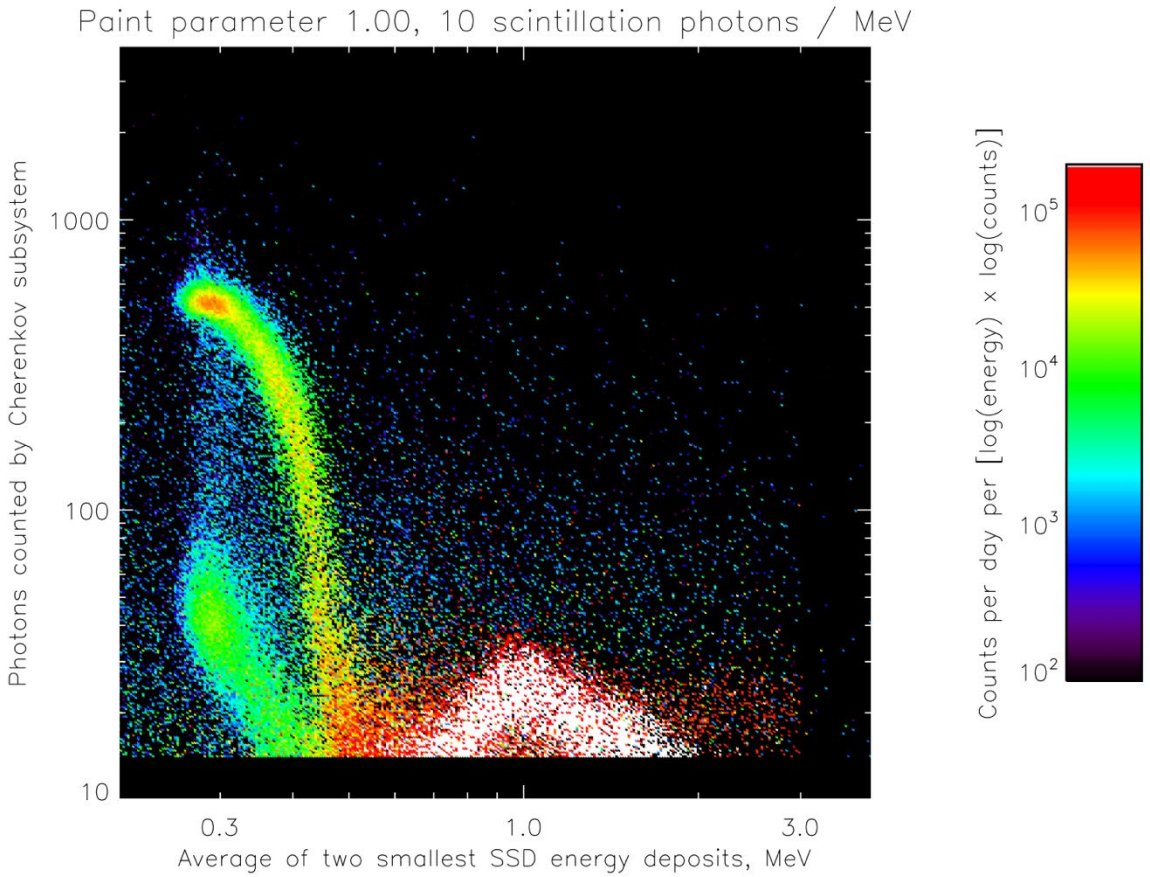

Figure 13. Distribution of Cherenkov counts vs. average of two smallest energy deposits per event in D1 through D8, for simulated events as in Figures 8 and 12. Paint parameter is 1.00 and scintillation yield is 10 photons per MeV.

However, since protons in the scintillation-dominated energy range are also those for which the SSDA gives good energy resolution (see Figure 3), we do not need to worry about the accuracy of the simulations' match to the CRA data here. Of more concern is the part of these plots with low CRA photon counts and minimum-two SSDA energy deposit around 0.45 MeV. This is where the forward and backward bands caused by sub-relativistic protons (the "necks") come together, and thus where a simulation that represents the flight data well can be used to quantify the effectiveness of our background-rejection algorithms. The shape of this merger region is affected by the paint parameter, as can be seen by comparing Figures 8 and 12, but it is also strongly affected by the scintillation yield. Figure 13 shows the simulated RPS response in the same form as before, for paint parameter of 1.00 and a too-low scintillation yield of 10 photons per MeV; comparing this with the observations in Figure 11, the two bands come together at too low a value of CRA photon counts, in fact below the bottom of the plot.

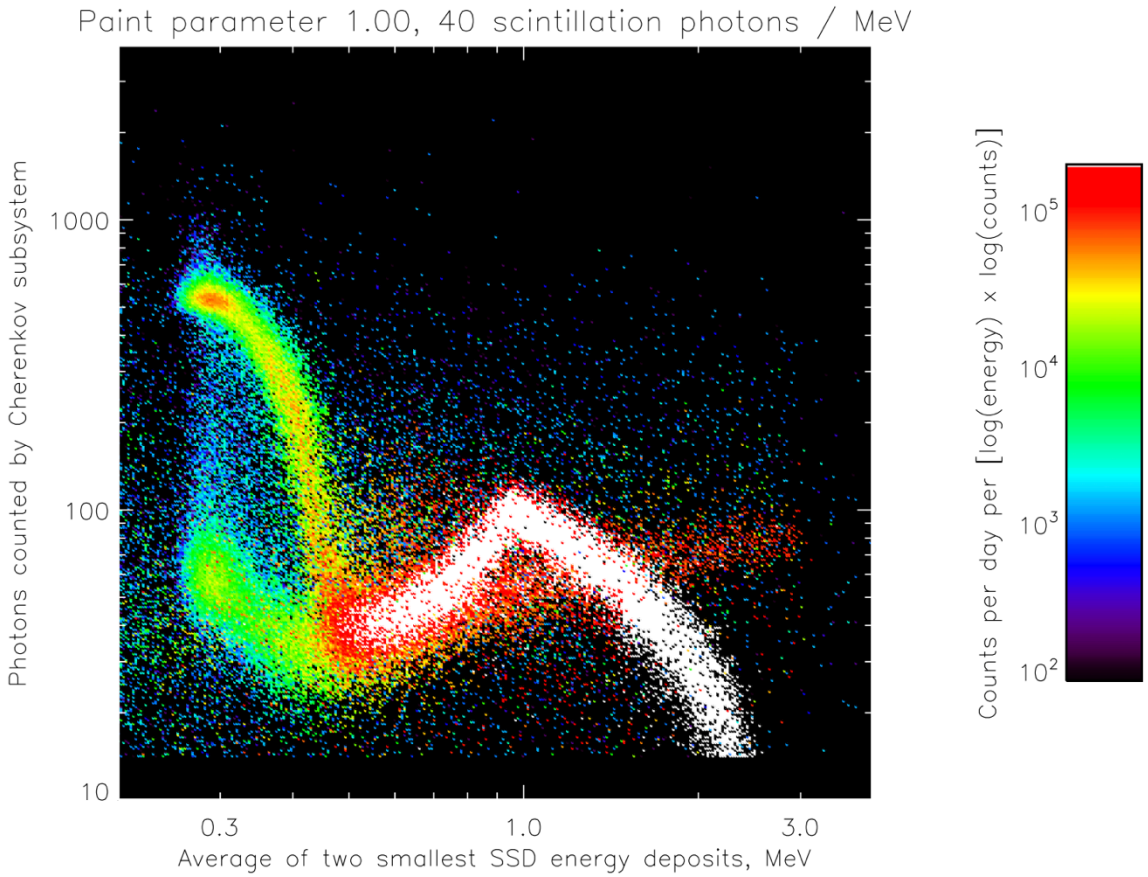

Figure 14. Distribution of Cherenkov counts vs. average of two smallest energy deposits per event in D1 through D8, for simulated events as in Figures 8, 12, and 13. Paint parameter is 1.00 and scintillation yield is 40 photons per MeV.

Figure 14 shows the simulated response with a scintillation yield of 40 photons per MeV. Here, the merging region is clearly at too high a value of CRA photon counts compared to the data in Figure 12.

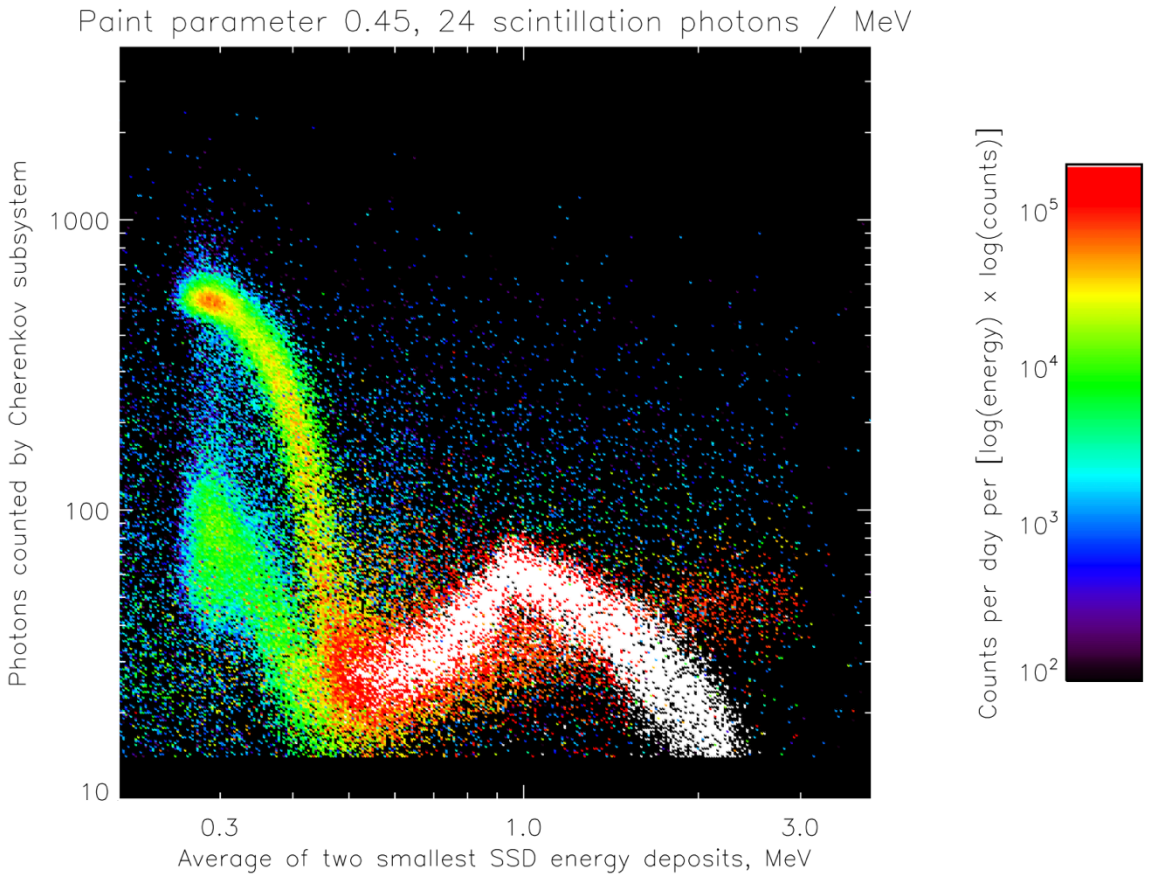

Figure 15. Distribution of Cherenkov counts vs. average of two smallest energy deposits per event in D1 through D8, for simulated events as in Figures 8 and 12 to 14. Paint parameter is 0.45 and scintillation yield is 24 photons per MeV, which are the values finally adopted as the best representation of the real sensor response.

Figure 15 shows a simulation with the values that we finally selected as the best match to the flight data: paint parameter of 0.45, scintillation yield of 24 photons per MeV. After defining cuts to reject as many events as possible that are not forward protons (section 5), we used the mapping from primary proton energy to CRA and SSD response as represented in Figure 15 to invert this relationship for the flight data, using the observed detector responses to infer proton energies, and also specifying uncertainties and quantifying contamination. This analysis is beyond the scope of this report and is discussed in the companion report [4]. Tabulations of the detailed energy and angular response of each of the proton energy channels in the RPS data release are available online; see [5].

5. Definition of Cuts to Select Forward-Going Protons

5.1 D1 vs. D8

Heretofore we have only considered the eight pulse-height-analyzed detectors of SSDA as an aggregate, using either the average of all eight energy deposits in an event or the average of the two smallest energy deposits in an event. However, we have access in the telemetry stream to all eight energy deposits, and we can use them to reject at least a few more backward-going protons. If a proton has an energy near the minimum necessary to penetrate the stack of solid-state detectors, it will lose most of its energy on the way through and, since dE/dx increases with decreasing proton energy, this means that it will deposit more energy in the last of the eight pulse-height-analyzed detectors that it crosses than in the first. For protons traversing the stack in the forward direction the first and last detectors will be D1 and D8 respectively, while backward-going protons will reverse this. Protons of higher energy will deposit less energy in all detectors, and the difference between energy deposited in different detectors will diminish because a smaller fractional decrease in the proton's energy and therefore a smaller increase in dE/dx will occur as the stack is traversed. We can use these trends to extract some directionality information to use as a cut.

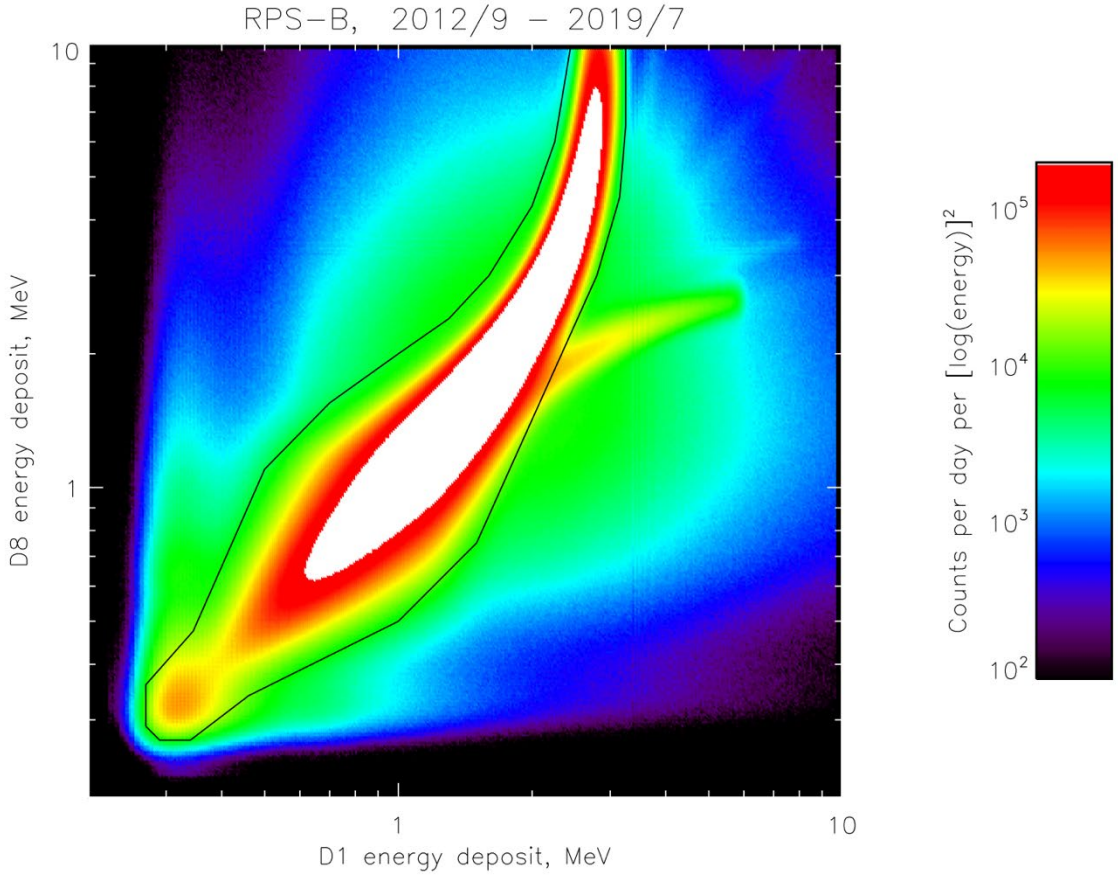

Figure 16. Distribution of D8 vs. D1 energy deposits for all events measured by RPS-B during the Van Allen Probes mission. Colorscale displays rate per bin, differential in the logarithm of D1 energy deposit and the logarithm of D8 energy deposit. Black line denotes the cut described in the main text that was used to select forward protons.

Figure 16 shows the distribution of event rates measured by RPS-B over different combinations of D1 and D8 pulse heights, summed over the entire Van Allen Probes mission. (The plot for RPS-A, which is not shown, looks very similar.) The trends described above can be seen: the dominant forward proton track starts with D1 energy deposit of about 3 MeV and D8 energy deposit saturated at 10 MeV, while higher-energy protons appear in the plot at lower values in both detectors and closer to the diagonal where they are equal. The fainter spur off to the right, symmetrical across the diagonal with the part of the track due to lower-energy forward protons, is the result of protons that go backward through the stack and lose most of their energy before reaching D1. To reject these, since they are not high enough in energy to emit directional Cherenkov light by which we can distinguish them from forward protons, we apply the cut shown as a black line in Figure 16, identifying events inside the polygon as forward-going protons to analyze further. The polygon used in the analysis is defined with straight lines in log-log space, as drawn here; the vertices in D1 are [0.27, 0.27, 0.345, 0.5, 0.7, 1.0, 1.3, 1.6, 2.0, 2.25, 2.45, 3.25, 3.25, 3.15, 2.8, 1.5, 1.0, 0.46, 0.34, 0.29] MeV, and in D8 are [0.29, 0.36, 0.475, 1.1, 1.55, 2.0, 2.4, 3.0, 4.3, 6.0, 10.0, 10.0, 6.5, 4.5, 3.0, 0.75, 0.5, 0.34, 0.27, 0.27] MeV.

5.2 CRA vs. SSDA

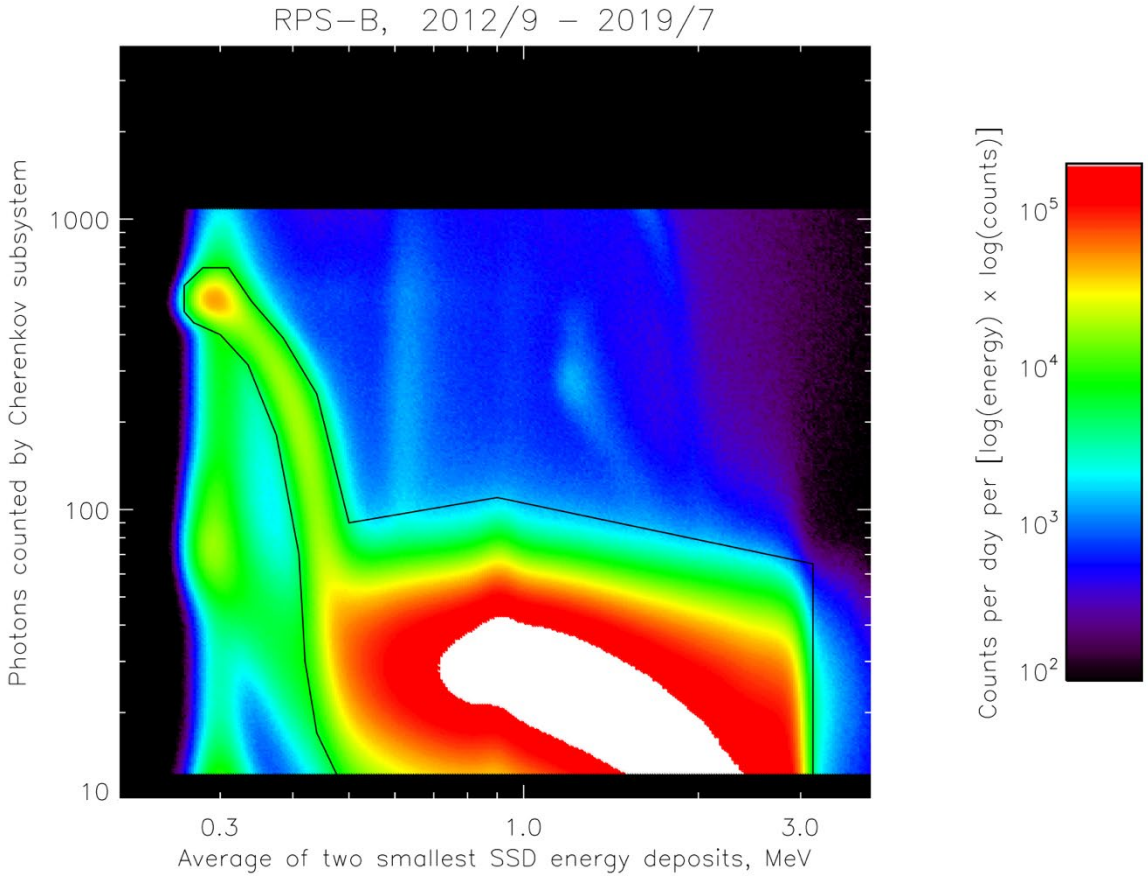

Figure 17. Distribution of Cherenkov counts vs. average of the two smallest energy deposits in D1 through D8 for all events measured by RPS-B during the Van Allen Probes mission. Black line denotes the cut described in the main text that was used to select forward protons.

Figure 17 is the same as Figure 11, showing distribution of RPS-B event rates vs. CRA photon counts and the average of the two smallest SSDA energy deposits, but for all events during the Van Allen Probes mission. The polygon shown as a black line defines the cuts that we used to select forward protons and reject, as much as possible, backward protons and other particles. (The greater statistics compared to Figure 11 show minor background populations more clearly, like the backward and forward GCR helium traces and the double-delta-ray vertical band at 0.6 MeV energy deposit, and with a faint vertical band at about 0.9 MeV appearing due to events in which three delta rays pass through the detector stack after being created by a proton that struck inert material but did not pass through the stack itself.) As in Figure 16, the polygon is defined with straight lines in log-log space joining vertices at [0.50, 0.44, 0.42, 0.41, 0.375, 0.335, 0.30, 0.27, 0.26, 0.26, 0.28, 0.31, 0.34, 0.385, 0.44, 0.50, 0.90, 3.15, 3.15] MeV of minimum-two energy deposit and [0.1, 17, 30, 70, 180, 315, 400, 440, 480, 590, 680, 680, 520, 390, 250, 90, 110, 65, 0.1] CRA photon counts.

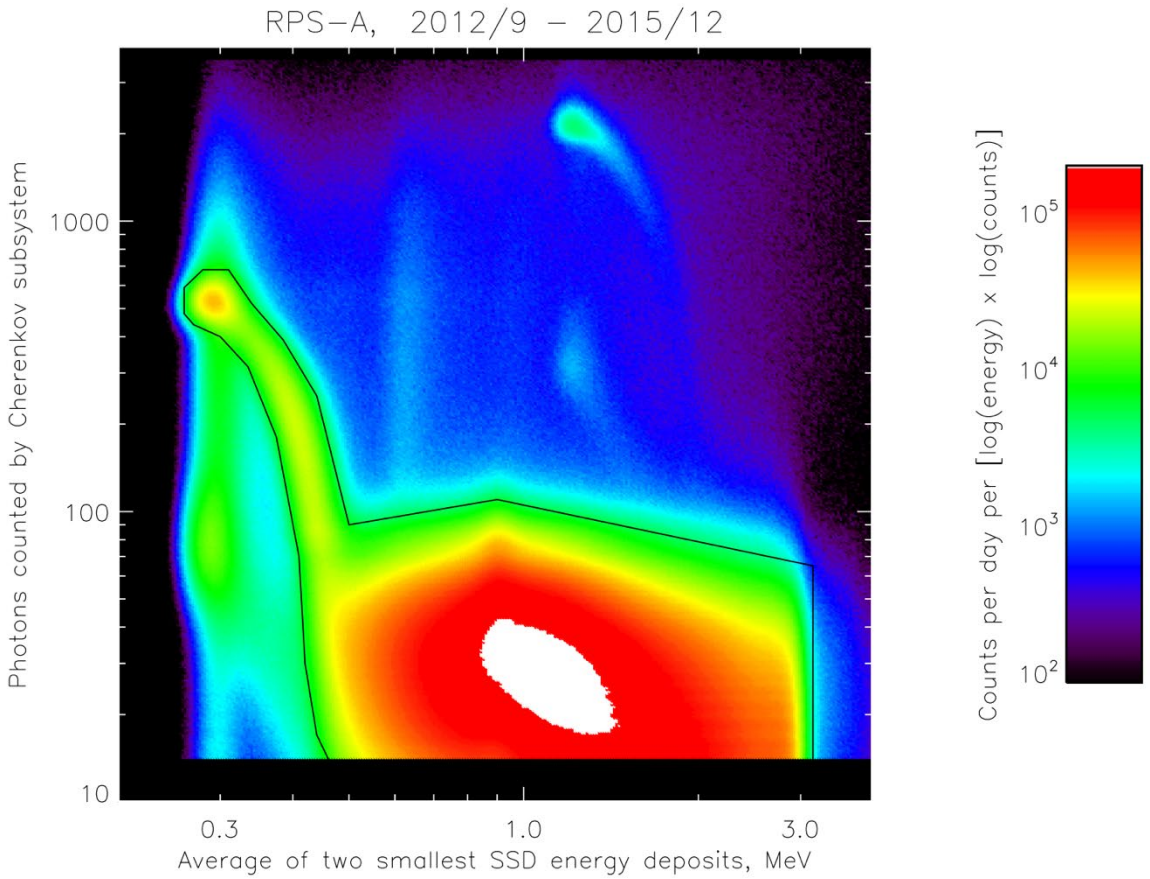

Figure 18. Distribution of Cherenkov counts vs. average of the two smallest energy deposits in D1 through D8 for all events measured by RPS-A before its CRA failed in early 2016.

Figure 18 shows the distribution of RPS-A event rates vs. CRA photon count and minimum-two SSD energy deposit, as in Figure 17 for RPS-B. The CRA of RPS-A failed early in 2016, as discussed by O'Brien et al. [4], so the statistics in this plot are not as great as in Figure 17. As noted with regard to Figures 9 and 10 above, the distribution of scintillation pulse heights for a given primary proton energy is looser for RPS-A than for RPS-B. Because we did not have a measurement-grounded basis for understanding the details of the differences in light production and collection between the two RPS units,

and between the flight data and the simulations, we did not have confidence that we could use the Cherenkov light output to estimate accurate energies for high-energy protons, as we had planned to do before launch. However, as discussed by O'Brien et al. [4], analysis of the minimum-two SSD energy deposit gave us satisfactory resolution of primary proton energies even up to around 1 GeV, and thus we ended up using the CRA data only for background rejection using these polygon cuts (and also for analysis of electrons, as discussed by Looper et al. [2]).

6. Adjustment of Gains Based on Flight Data

6.1 Solid-State Detectors

As discussed at the start of this report, the determination of the calibration of the RPS detectors was an iterative process throughout the Van Allen Probes mission. As such, the process has been described not chronologically as it occurred, with many loopbacks and revisions, but topically; in particular, the plots of flight data in Figures 9 to 12 and 16 to 18 were made using the final simulation-based calibrations presented in this section, and such things as the polygon cuts discussed in section 5 are presented in their final form. The CRA corrections discussed in section 6.2, and used in the preceding plots, were actually one of the last pieces of the calibration puzzle that was put in place: they were not finalized until after the end of the actual spacecrafts' lives, and they were not incorporated into the RPS data releases until CDF version 1.3.

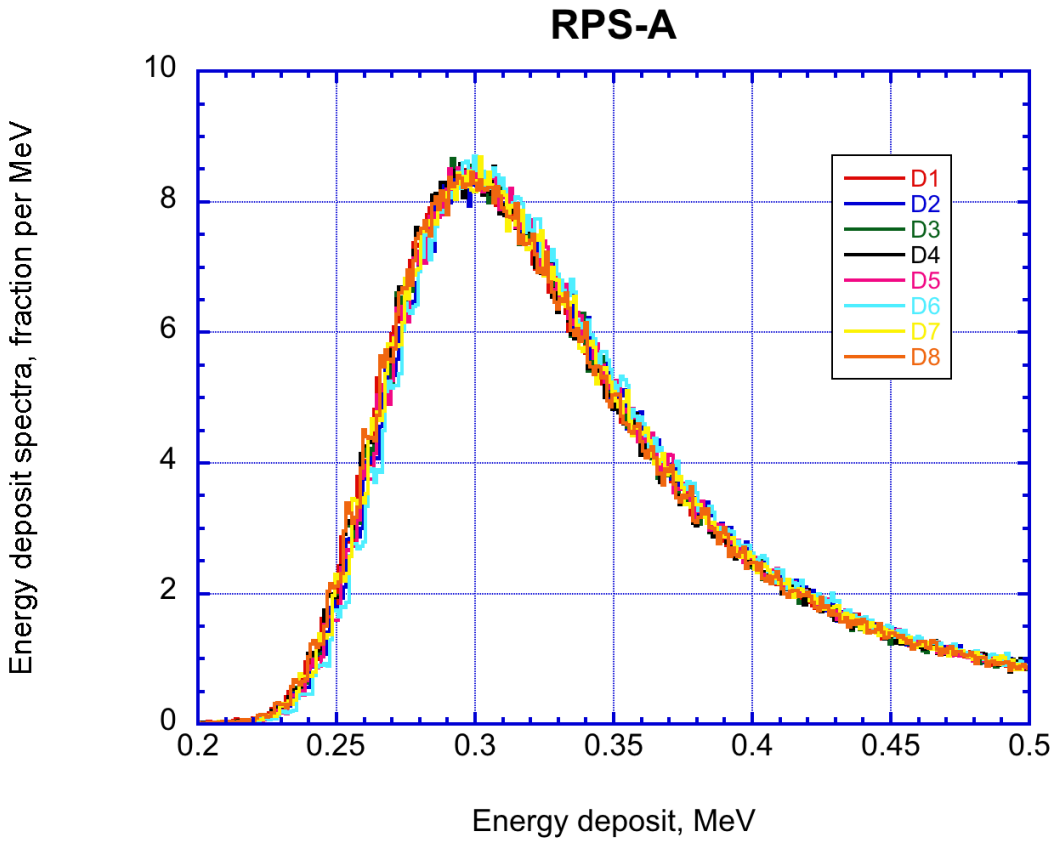

Figure 19. Energy-deposit spectra for forward-going relativistic protons, those with CRA photon counts between 400 and 650 per particle event, that were observed by RPS-A for the first ten months of the mission.

On the other hand, early in the mission it became clear that the simulations were predicting a higher energy deposit in the solid-state detectors for relativistic protons than the values reported for either RPS unit in the flight data. Moreover, as seen in Figure 19, some detectors' energy-deposit spectra were systematically displaced relative to the others'. Figure 19 shows the distributions of energy deposits in each of the eight detectors of RPS-A for the first ten months of the mission, restricted to events with between 400 and 650 CRA photon counts. A plot like this for the simulations (not shown) would have the

peaks displaced to the right, and would have all eight curves identical within statistical error, as expected for these extremely penetrating particles.

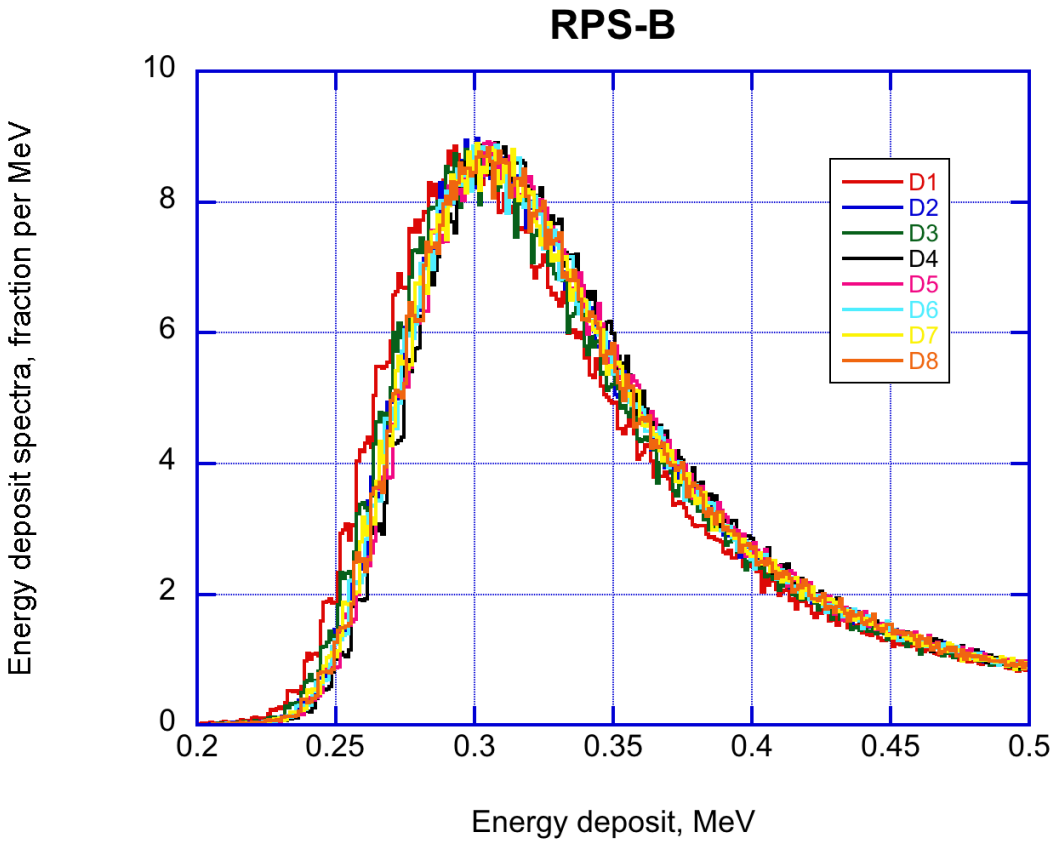

Figure 20. Energy-deposit spectra for forward-going relativistic protons, those with CRA photon counts between 400 and 650 per particle event, that were observed by RPS-B for the first ten months of the mission.

Figure 20 shows the same energy-deposit spectra for RPS-B, with even more pronounced systematic differences between the curves. We never did arrive at a conclusion as to the reason that the idealized detector response in the simulations (detectors exactly 1 mm thick, with no dead layers, and with "telemetry" representing exact tabulation of all energy deposit) differed from the measured values: there could have been dead layers or charge-collection issues that biased the measurements of the very short-range alpha particles used to derive the calibration discussed in section 3.1, or the detectors might not have been exactly 1 mm thick, or there might have been some error in our understanding of the circuitry that digitized the detector outputs so that extrapolation outside the energy range probed by the alphas was not valid. All seemed unlikely for various reasons; however, relativistic protons' energy deposit is a well-understood matter of basic physics, and so we decided to devise a revised calibration to replace the gains and offsets in Table 1 for some purposes, in effect mapping the real sensor responses onto the scale given by the simulations.

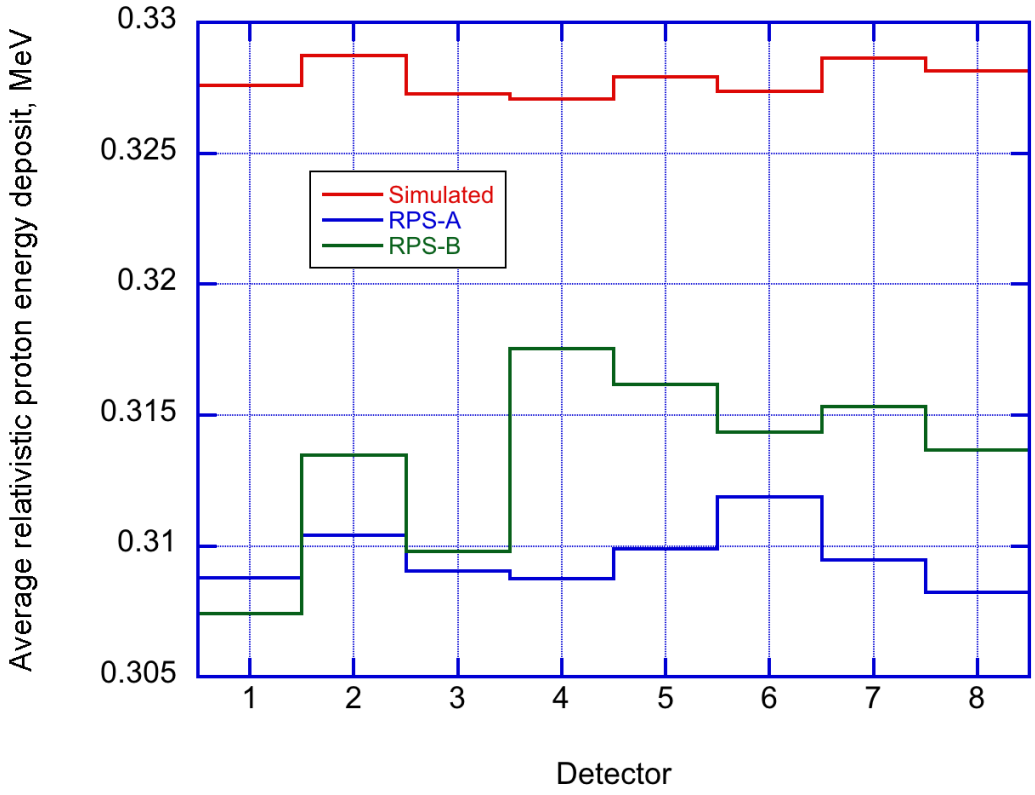

Figure 21. Average energy of peak of energy-deposit spectrum in each detector for forward-going relativistic protons, those with CRA photon counts between 400 and 650 per particle event. Observations are from the first ten months of mission.

Figure 21 shows the average energy deposit between the half-maximum points of the curves for each detector in Figures 19 and 20, and for the simulations (spectra not shown in earlier figures). The offset toward lower values for the observations is clear, as is the fact that variations between detectors are greater for the real data than the statistical fluctuations visible for the simulations.

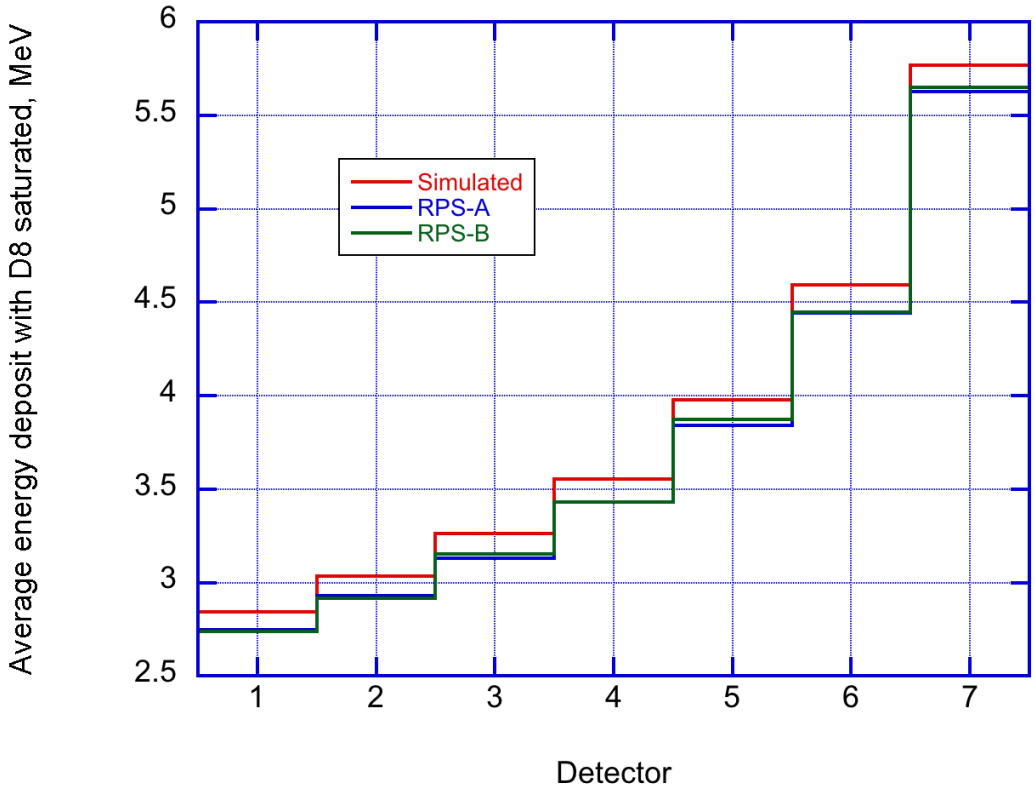

Figure 22. Average energy deposit in detectors D1 to D7 for events with D8 saturated. Observations are from the first ten months of mission.

In order to determine a revision to the linear calibration in Table 1, we needed two points for each detector; the position of the peak for relativistic protons as in Figure 21 provided one, and for the other we went to the other extreme, looking at the average energy deposit in each detector D1 through D7 for those events where D8 is saturated (actually slightly below saturation at 9.7 MeV, so that we did not lose events when gain changes due to temperature fluctuations shifted the saturation level slightly). In Figure 16, these would be the events where the forward-proton track crosses the top of the plot at a D1 energy deposit around 2.7 MeV. Figure 22 shows the average energy deposits of these events for data taken early in the mission, along with the values from the simulations; an offset of the flight data from the simulations, similar in all detectors, is visible. We need such a second point for D8 as well; simply assuming that the offset between data and simulations was the same as the average in Figure 22 for D1 to D7, we mapped 9.7 MeV in the simulations to 9.7 MeV minus 0.14 MeV in the data for each spacecraft.

Table 4. SSDA Gains and Offsets Determined by Rescaling to Match Simulations, in Units of MeV/Channel and MeV Respectively.

Detector	RPS-A gain	RPS-A offset	RPS-B gain	RPS-B offset
D1	0.006666326	0.05315223	0.006691855	0.05350441
D2	0.006698962	0.05416242	0.006735900	0.05782391
D3	0.006725986	0.05165412	0.006738977	0.02193629
D4	0.006695923	0.05292184	0.006715937	0.05301029
D5	0.006666139	0.05319168	0.006667559	0.05332874
D6	0.006674405	0.05324131	0.006690197	0.05661310
D7	0.006615704	0.05358268	0.006608464	0.05777105
D8	0.006543851	0.06111138	0.006569961	0.05809350

Table 3 gives the values that replace those in Table 1 under the new calibration. It should be noted that we use Table 1 to convert PHA channels to MeV of energy deposit for the data released as CDFs, because that is directly traceable to the hardware (alpha source, onboard electronics). However, since we used the simulations to decide what events to discard as background and to map the minimum-two SSD value to an estimate of the primary proton energy, as detailed by O'Brien et al. [4], we use the values in Table 3 substituted into the equations above Table 1 (we did not alter the temperature correction) to obtain the values of energy deposit that are used to apply the polygon cuts described in section 5 and to estimate proton energies for those events accepted by the cuts.

6.2 Cherenkov Subsystem

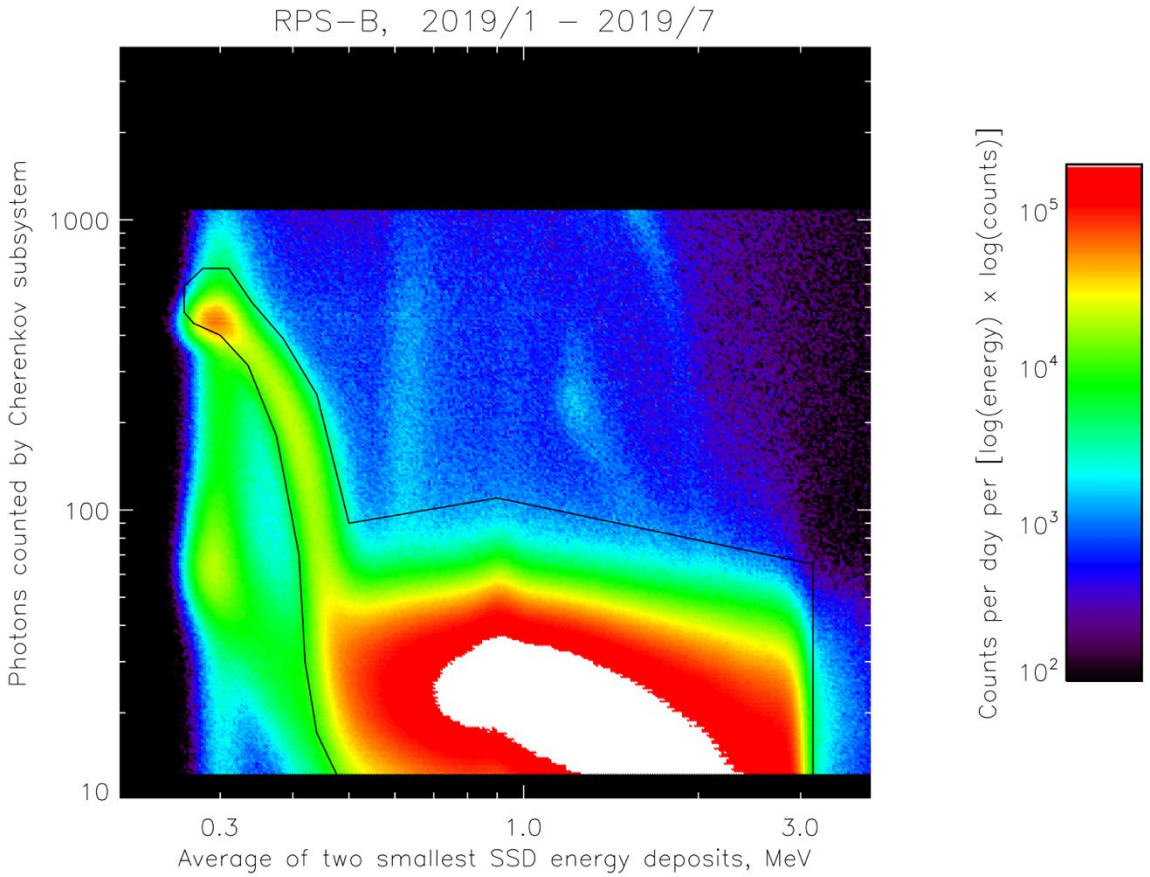

Figure 23. Distribution of Cherenkov counts vs. average of the two smallest energy deposits in D1 through D8 for all events measured by RPS-B during its last seven months of operation, without correction of gain for temperature and temporal drift.

As noted in section 3.2 above, we did not initially derive a temperature correction for the conversion of pulse heights from the Cherenkov subsystem to photon counts. As the mission went on, however, it became clear that there was a significant temperature dependence to the gain of the MCP in both RPS units and, moreover, that over the duration of the mission there was a noticeable overall loss of gain with time. Figure 23 shows the effect of the accumulated gain changes on RPS-B data: this is the same kind of plot as in Figure 17, showing the polygon cut that we applied to CRA photon counts vs. minimum-two SSD energy deposits, but showing only data taken near the end of the mission and omitting the gain corrections described below (which were applied in creating Figure 17). Clearly the relativistic forward proton response has sagged so that a significant fraction is below the black line, indicating that numerous valid high-energy proton events would be rejected by that cut.

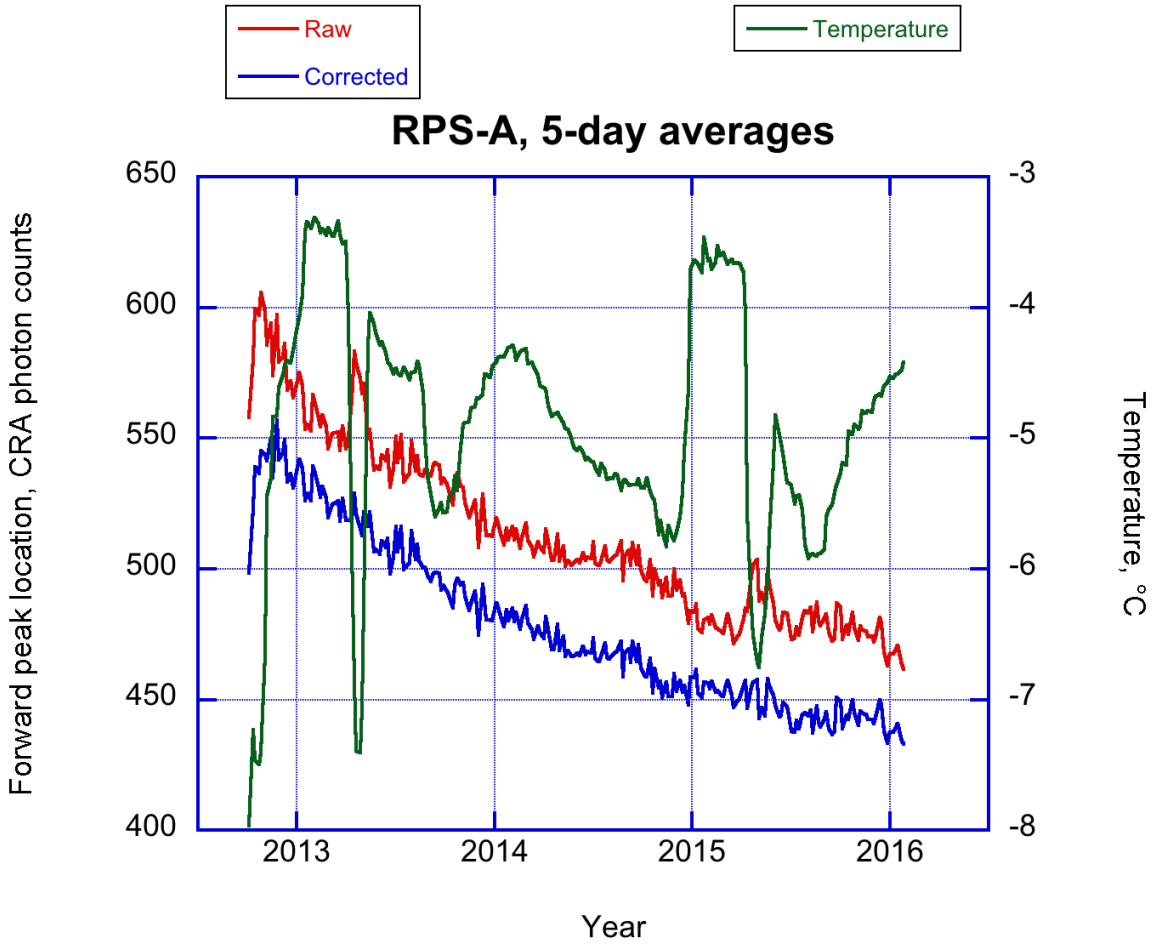

Figure 24. 5-day averages of RPS-A temperature (right vertical axis) together with the average measured CRA photon counts in the forward relativistic proton peak (left vertical axis), both with and without temperature correction as described in main text.

Figure 24 shows the effect of temperature variations on the MCP gain of RPS-A. The red curve labeled "Raw" is the average value of CRA photon counts for all events in a 5-day period due to relativistic forward protons with a minimum-two energy deposit between 0.285 MeV and 0.305 MeV, showing variations that are anticorrelated with the temperature shown in green. A linear temperature correction analogous to that for the solid-state detectors in section 3.1 was devised, as will be described below, and when applied to the Raw data it gives the blue "Corrected" curve for the position of the forward proton peak, which has a much simpler temporal drift.

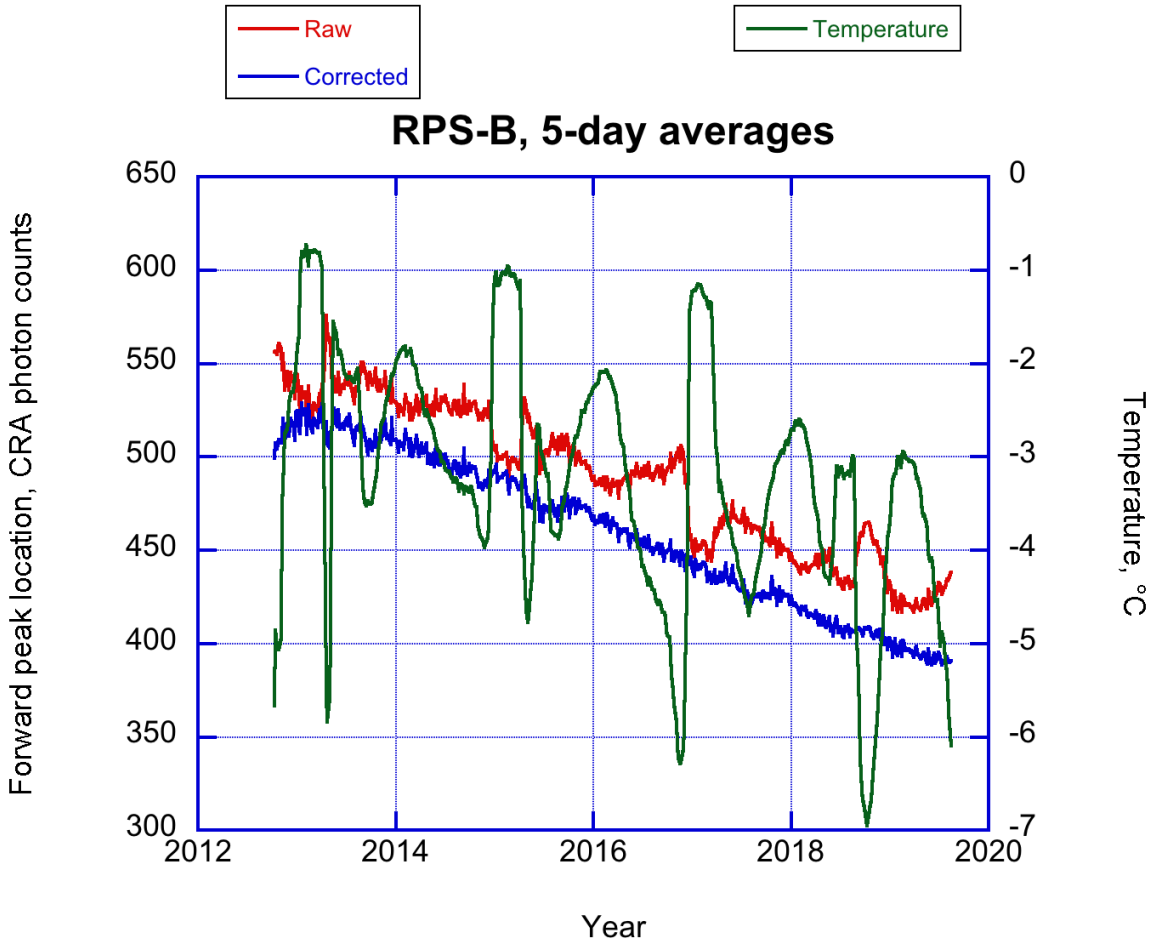

Figure 25. 5-day averages of RPS-B temperature (right vertical axis) together with the average measured CRA photon counts in the forward relativistic proton peak (left vertical axis), both with and without temperature correction as described in main text.

Figure 25 shows the same temperature trend and its correction for RPS-B, again as 5-day averages. RPS-B experienced more and wider temperature swings than did RPS-A, so the effects on the "Raw" curve are more pronounced than in Figure 24.

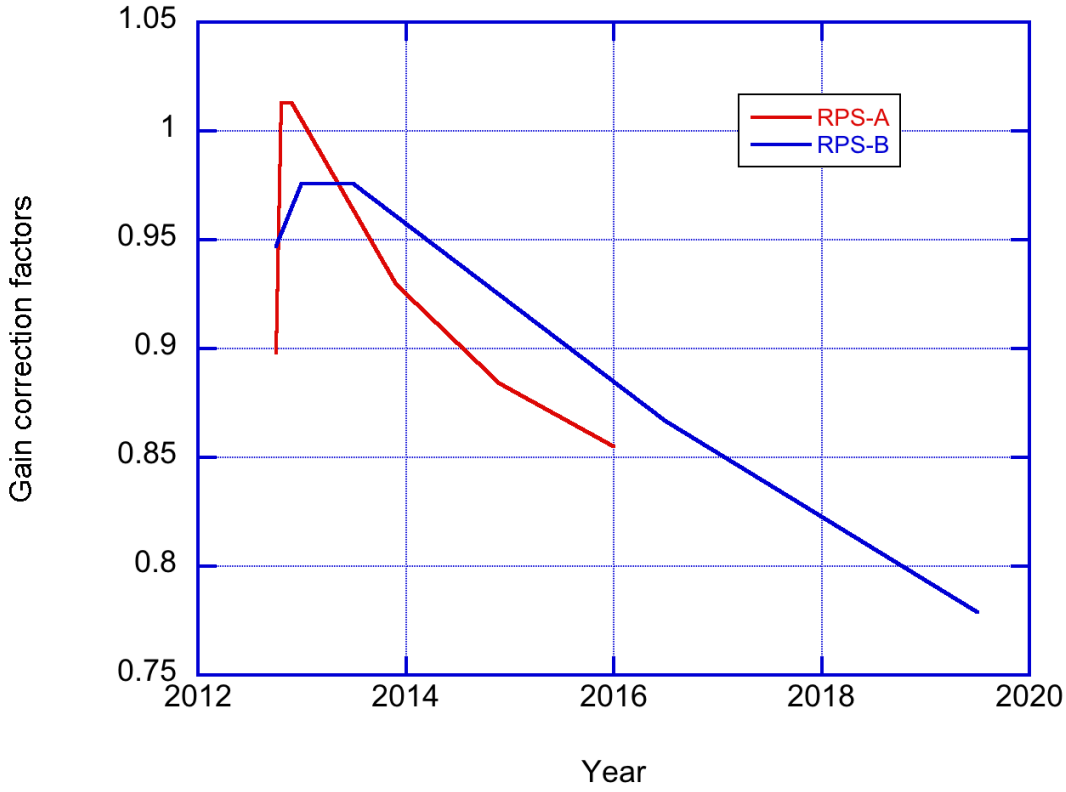

Figure 26. Correction factors for temporal gain drift of RPS-A and RPS-B, as described in the main text.

Figure 26 shows the piecewise-linear correction factors that were adopted to correct for the temporal gain drift of each sensor's MCP. In all, the equations above Table 2 were amended as follows (gain and offset were not changed from those in Table 2):

$$D_9 = \frac{c_9 + H_9 g_9}{[1 + X\bar{T}(t)]Y(t)}$$

$D_9 =$ Cherenkov photon count
$c_9 =$ Offset, photons
$g_9 =$ Gain, photons/channel
$H_9 =$ Pulse height for CRA, channel
$X =$ Temperature coefficient, 1/°C
$\bar{T}(t) =$ Daily-averaged temperature, °C
$Y(t) =$ Drift factor

Table 5. CRA Gains (Photons/Channel), Offsets (Photons), and Temperature Coefficients (Fraction per °C)

Parameter	RPS-A	RPS-B
c_9	7.42765	8.705149
g_9	2.649163	0.7694737
X	-0.015	-0.02

We found that, because of the coarse digitization of temperature in the telemetry, a daily average value $\bar{T}(t)$ gave the best results for the temperature correction without introducing spurious intraday variations due to digitization that were much larger than the changes of the average from day to day. (For the same reason, we also changed the SSDA temperature correction given in section 3.1 to use the daily-averaged temperature starting with version 1.3 of the CDF, though this makes much less difference since the coefficient is much smaller than for CRA.) The drift factor $Y(t)$ is the quantity plotted in Figure 26; the values for each day are linearly interpolated between or extrapolated from the values [0.898, 1.013, 1.013, 0.930, 0.884, 0.855] at decimal year points [2012.75, 2012.8, 2012.9, 2013.9, 2014.9, 2016.0] for RPS-A, and [0.947, 0.976, 0.976, 0.867, 0.779] at decimal years [2012.75, 2013.0, 2013.5, 2016.5, 2019.5] for RPS-B.

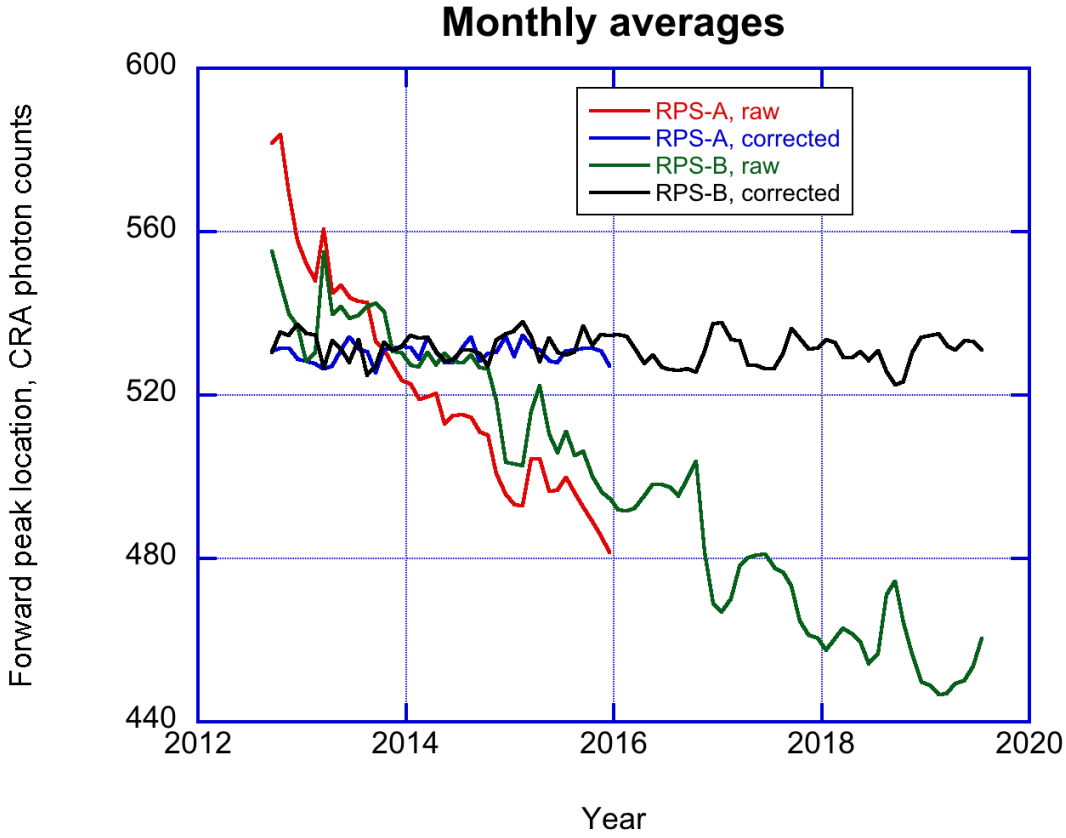

Figure 27. Monthly-averaged CRA photon counts in the forward relativistic proton peak measured aboard both RPS units over the lifespans of their CRA subsystems, both raw and with the corrections described above applied.

Figure 27 shows the results of the application of these corrections for both RPS units, with the temporal trends and temperature-anticorrelated peaks and dips greatly smoothed out. This meant that each sensor's data throughout the lifespan of its CRA subsystem (that of RPS-A failed in early 2016) were scaled commensurately, and we could apply the fixed polygon cuts described in section 5.2 with consistent results. The tight vertical concentration of the points due to relativistic protons in the plots shown in Figures 17 and 18, which were produced with these corrections applied, demonstrates the success of the gain correction algorithms described herein.

7. References

[1] Allison, J. et al., "Recent Developments in Geant4," *Nucl. Inst. and Meth. In Phys. Res. A*, **835**, 186-225, doi: 10.1016/j.nima.2016.06.125. 2016.

[2] Looper, M. D.; T. P. O'Brien; and J. E. Mazur, *Relativistic Proton Spectrometer Electron Response*, Aerospace Report Number ATR-2021-02026, The Aerospace Corporation, El Segundo, CA, 2021.

[3] Mazur, J. E.; A. Lin; D. Mabry; N. Katz; Y. Dotan; J. George; J. B. Blake; M. Looper; M. Redding; T. P. O'Brien; J. Cha; A. Birkitt; P. Carranza; M. Lalic; F. Fuentes; R. Galvan; and M. McNab, "The Relativistic Proton Spectrometer (RPS) for the Radiation Belt Storm Probes Mission," *Space Sci. Rev*. **179** (1-4), 221-261, doi: 10.1007/s11214-012-9926-9. 2013.

[4] O'Brien, T. P.; M. D. Looper; J. E. Mazur; and E. L. Mazur (2021), *Relativistic Proton Spectrometer Flux Determination and Data Products*, Aerospace Report Number ATR-2021-02018, The Aerospace Corporation, El Segundo, CA. 2021.

[5] O'Brien, T. P.; M. D. Looper; and J. E. Mazur, Sensor Response Files for the Relativistic Proton Spectrometer aboard NASA's Van Allen Probes, zenodo.org, doi:10.5281/zenodo.5502043. 2021.

[6] Viehmann, W. et al., "Photomultiplier Window Materials Under Electron Irradiation: Fluorescence and Phosphorescence," *Appl. Opt*. **14** (9), 2104-2115, doi: 10.1364/AO.14.002104. 1975

Appendix A. Optical Parameters Used in Simulation of CRA Response

A.1 Materials Considered

In the Geant4 simulations, optical photons were generated in the Cherenkov radiator and in the faceplate of the PMT, and the transmission and reflection of photons exiting these materials into the surrounding vacuum was also modeled. The radiator was made of magnesium fluoride, and the PMT faceplate was made of UV-grade fused silica, so in order to enable Geant4 to simulate these photons several properties of these two materials had to be specified in the code. In addition, as described in section 4.1, black paint was applied to the small end of the radiator to suppress detection of Cherenkov light from backward-going particles; this was modeled, as detailed there, as "black MgF_2," which had the same refractive index profile as MgF_2 (adjusted by the "paint parameter" in later simulations) but a very short absorption length of 1 μm across the entire range of wavelengths. The photocathode on the back of the faceplate needed to accept photons reaching it through the faceplate without internal reflection, but then needed to stop them, and so it was made of "black fused silica" related in the same way to fused silica. (The microchannel plate itself at the back of the PMT was not used in the tracking of optical photons, but we modeled its material as fused quartz to give it about the right amount of mass for the minor degree of shielding it provided.)

A.2 Refractive Indices vs. Wavelength

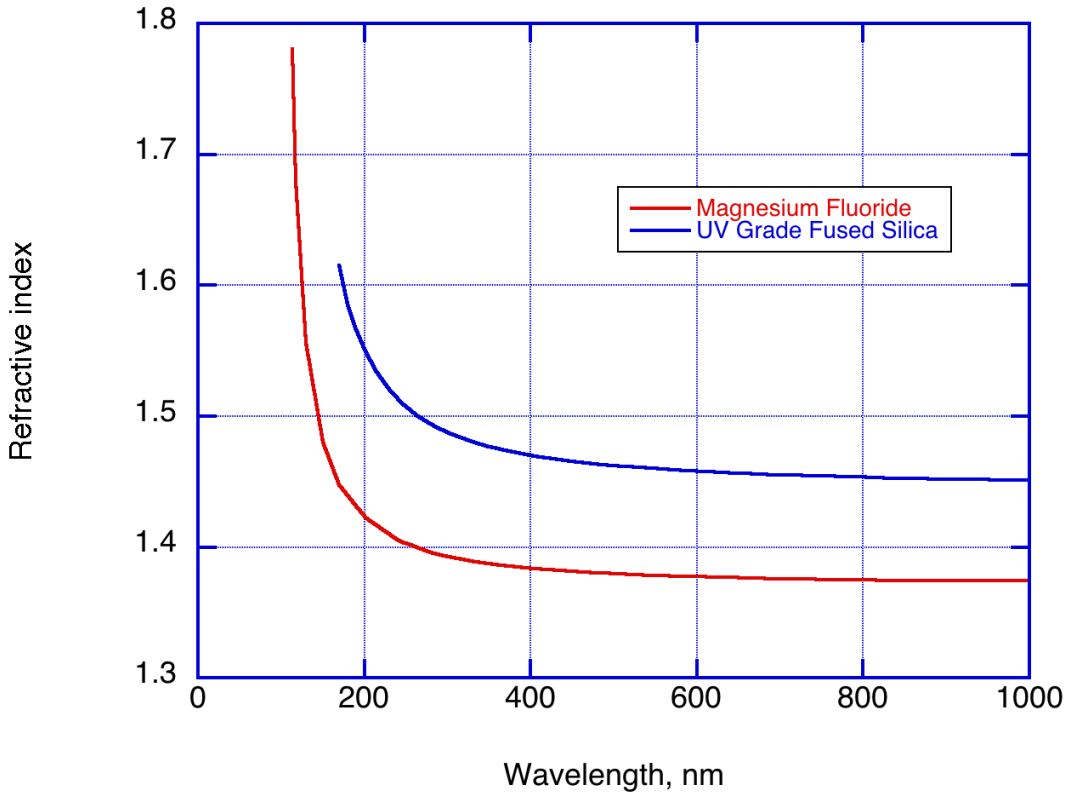

Figure 28. Refractive indices as functions of photon wavelength of optical materials used in the Geant4 simulation.

Figure 28 shows the refractive indices assigned to the two optical materials in the simulation as a function of wavelength. The values for MgF_2 were obtained from Corning (originally retrieved from http://www.corningcn.com/docs/specialtymaterials/pisheets/H0607_MgF2_Product_Sheet.pdf), and those

for fused silica from Melles Griot (originally retrieved from http://www.mellesgriot.com/products/optics/mp_3_2.htm).

A.3 Absorption Lengths vs. Wavelength

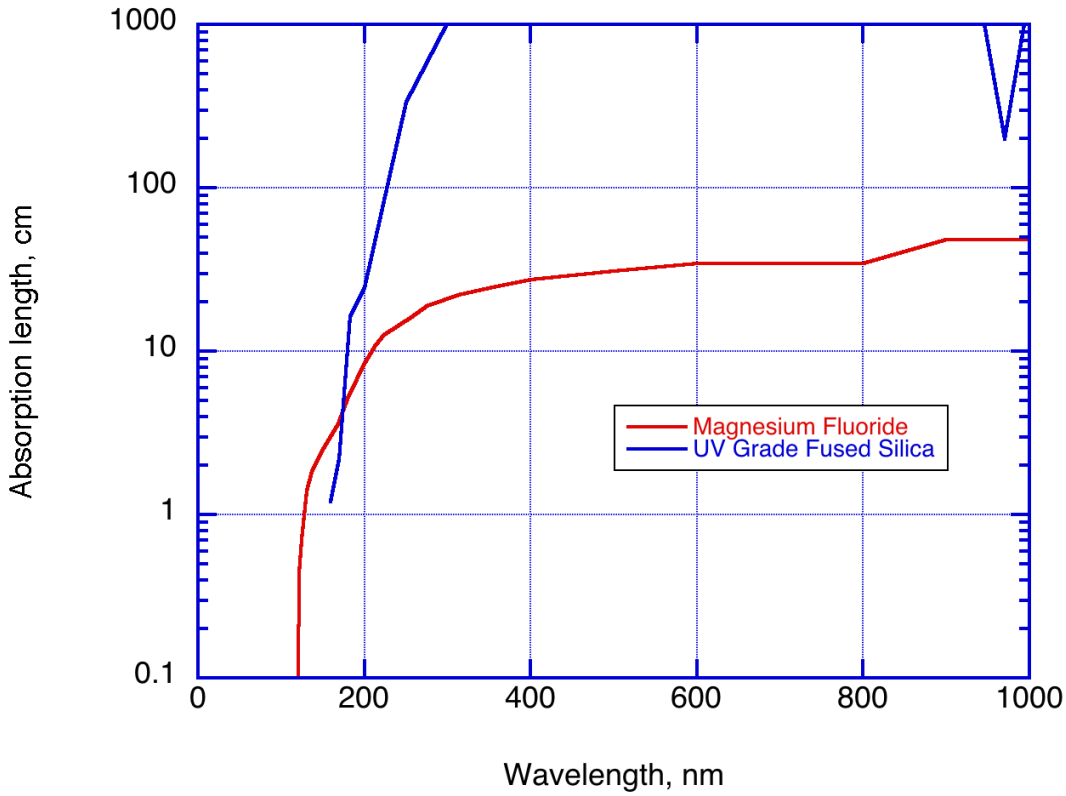

Figure 29. Absorption lengths as functions of photon wavelength of optical materials used in the Geant4 simulation.

Figure 29 shows the absorption lengths assigned to the two optical materials in the simulation as a function of wavelength. The values for MgF_2 were obtained from Janos Technology (originally retrieved from http://www.janostech.com/knowledge_center/mgf_material.html) and those for fused silica from Melles Griot (originally retrieved from http://www.mellesgriot.com/products/optics/mp_3_2.htm).

A.4 Scintillation Spectrum in Magnesium Fluoride

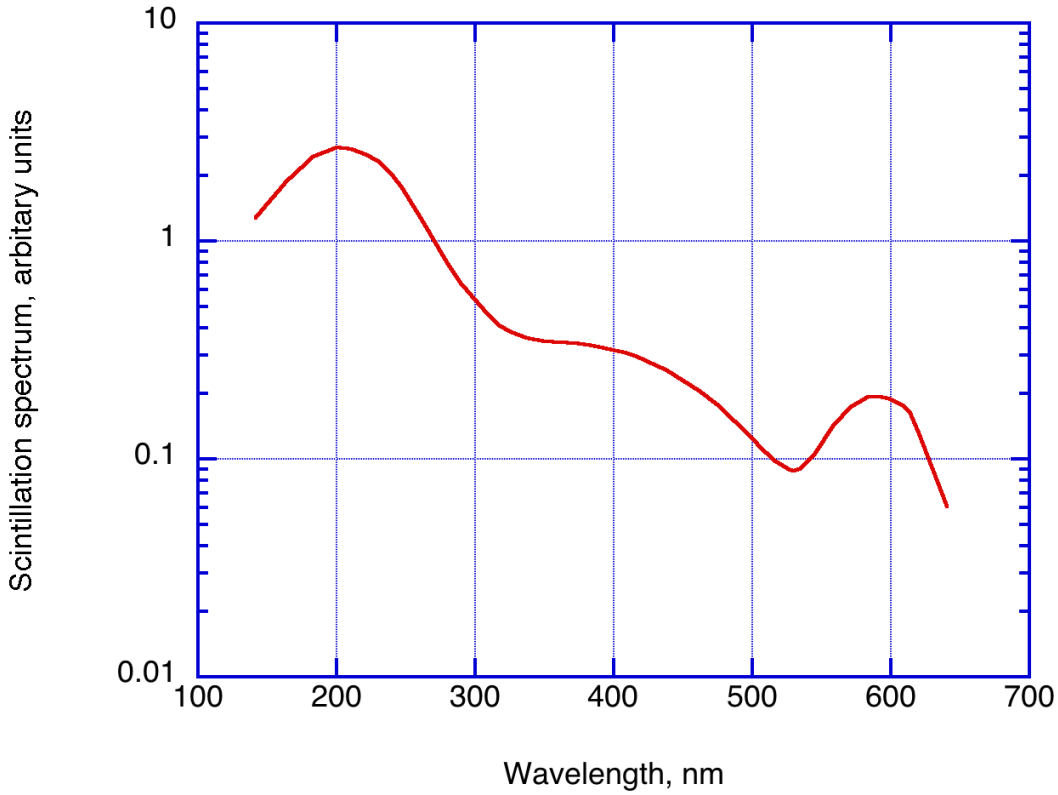

Figure 30. Shape of scintillation spectrum of MgF_2 as used in the Geant4 simulation.

As discussed in section 4.2, we took the scintillation yield in MgF2 as an adjustable parameter. The spectral distribution according to which the simulated scintillation photons were generated is shown in Figure 30, which was obtained from Viehmann et al. [6]. We did not model any scintillation in the PMT faceplate because the pathlength of particles through its thickness of 2 mm would be much shorter than their pathlength through the 50 mm thickness of the radiator, and because Viehmann et al. [6] found the scintillation yield of fused quartz to be several times smaller than that of MgF_2.

A.5 Quantum Efficiency of Photomultiplier

Burle Industries, the manufacturer of the PMTs used in RPS, marked as proprietary the plot that they sent to us of the quantum efficiency of their Planacon 85001 PMTs, so it will not be reproduced here. The values used in the simulation were very similar to those presently available (creation of free Photonis user account required) on the datasheet at https://www.photonis.com/system/files/2019-04/PLANACON-10µm-32x32-datasheet.pdf, or somewhat less similar to the curve for the S20 photocathode (about 20% at 400 nm) plotted at https://www.photonis.com/products/hi-qe-photocathodes.

A.6 Spatial Uniformity of Photomultiplier Response

The brochure for the Burle Planacon 85001 PMT specified that uniformity of response across the faceplate would be 1:1.5 or better. We did not have the means to measure this, but we were provided with

a graph of a typical uniformity scan from such a device. We approximated this by drawing a parabolic curve of efficiency from 0.667 at one edge through 1.00 at the center and back to 0.667 at the other edge; we did this in both directions across the faceplate, and took the lesser of the two values calculated thus for each point on the faceplate. We thought that we might see a difference in the simulations between the probability distributions of photon counts for protons coming down the sensor boresight and for those that just grazed the inside of the radiator crystal. However, the light from any subset of the protons was spread so broadly across the faceplate that we never saw any discernible difference between subsets, so we took this parabolic pattern to be a good enough representation of the pattern of nonuniformity.

AEROSPACE REPORT NO.
ATR-2021-02025

Relativistic Proton Spectrometer Detector Calibration

Cognizant Program Manager Approval:

Robert D. Rutledge, DIRECTOR - DEPARTMENT
SPACE SCIENCE APPLICATIONS LABORATORY
PHYSICAL SCIENCES LABORATORIES
ENGINEERING & TECHNOLOGY GROUP

Aerospace Corporate Officer Approval:

Todd M. Nygren, SENIOR VP ENGINEERING & TECHNOLOGY
OFFICE OF EVP

Content Concurrence Provided Electronically by:

Mark D. Looper, RESEARCH SCIENTIST
MAGNETOSPHERIC & HELIOSPHERIC SCIENCES
SPACE SCIENCES DEPARTMENT
ENGINEERING & TECHNOLOGY GROUP

Office of General Counsel Approval Granted Electronically by:

Alex D. Konde, ATTORNEY
OFFICE OF THE GENERAL COUNSEL
OFFICE OF GENERAL COUNSEL & SECRETARY

SY0875

AEROSPACE REPORT NO.
ATR-2021-02025

Relativistic Proton Spectrometer Detector Calibration

Export Control Office Approval Granted Electronically by:

Angela M. Farmer, SECURITY SUPERVISOR
GOVERNMENT SECURITY
SECURITY OPERATIONS
OFFICE OF THE CHIEF INFORMATION OFFICER

SY0875